

Integrated behavioural analysis of FRP-confined circular columns using FEM and machine learning

Liaqat Ali^a, Haytham F. Isleem^b, Alireza Bahrami^{c,*}, Ishan Jha^d, Guang Zou^a, Rakesh Kumar^e, Abdellatif M. Sadeq^f, Ali Jahami^g

^a Department of Ocean Science and Engineering, Southern University of Science and Technology, Shenzhen, China

^b School of Applied Technologies, Qujing Normal University, Qujing 655011, Yunnan, China

^c Department of Building Engineering, Energy Systems and Sustainability Science, Faculty of Engineering and Sustainable Development, University of Gävle, 801 76 Gävle, Sweden

^d Department of Civil Engineering, Indian Institute of Technology-BHU, Varanasi, Uttar Pradesh, India

^e Department of Civil Engineering, National Institute of Technology Patna, India

^f Mechanical and Industrial Engineering Department, Qatar University, Doha, Qatar

^g Faculty of Engineering, University of Balamand, Tripoli P.O. Box 100, Lebanon

ARTICLE INFO

Keywords:

Confined concrete
Double steel tube
Finite element model
FRP reinforcement
Strength enhancement
Machine learning

ABSTRACT

This study investigates the structural behaviour of double-skin columns, introducing novel double-skin double filled tubular (DSDFT) columns, which utilise double steel tubes and concrete to enhance the load-carrying capacity and ductility beyond conventional double-skin hollow tubular (DSHT) columns, employing a combination of finite element model (FEM) and machine learning (ML) techniques. A total of 48 columns (DSHT+DSDFT) were created to examine the impact of various parameters, such as double steel tube configurations, thickness of fibre-reinforced polymer (FRP) layer, type of FRP material, and steel tube diameter, on the load-carrying capacity and ductility of the columns. The results were validated against the experimental findings to ensure their accuracy. Key findings highlight the advantages of the DSDFT configuration. Compared to the DSHT columns, the DSDFT columns exhibited remarkable 19.54 % to 101.21 % increases in the load-carrying capacity, demonstrating improved ductility and load-bearing capabilities. Thicker FRP layers enhanced the load-carrying capacity up to 15 %, however at the expense of the reduced axial strain. It was also observed that glass FRP wrapping displayed 25 % superior ultimate axial strain than aramid FRP wrapping. Four different ML models were assessed to predict the axial load-carrying capacity of the columns, with long short-term memory (LSTM) and bidirectional LSTM models emerging as superior choices indicating exceptional predictive capabilities. This interdisciplinary approach offers valuable insights into designing and optimising confined column systems. It sheds light on both double-tube and single-tube configurations, propelling advancements in structural engineering practices for new constructions and retrofitting. Further, it lays out a blueprint for maximising the performance of the confined columns under the axial compression.

Notations

<i>FEM</i>	Finite element model
<i>ML</i>	Machine learning
<i>FRP</i>	Fibre-reinforced polymer
<i>DSDFT</i>	Double-skin double filled tubular
<i>DSHT</i>	Double-skin hollow tubular
<i>CFFT</i>	Concrete-filled FRP tube
<i>GFRP</i>	Glass fibre-reinforced polymer

<i>AFRP</i>	Aramid fibre-reinforced polymer
σ	Stress
ε	Strain
f_{cc}	Peak confined concrete strength
ε_{cc}	Confined concrete strain at peak strength
R_{σ}	Stress ratio
R_{ε}	Strain ratio
f_c	Unconfined concrete strength
E_{cc}	Elastic modulus of confined concrete

* Corresponding author.

E-mail address: alireza.bahrami@hig.se (A. Bahrami).

<https://doi.org/10.1016/j.jcomc.2024.100444>

f_r	Residual stress
ψ	Dilation angle
E_{frp}	Elastic modulus of FRP
t_{frp}	Thickness of FRP
h	Inner depth of FRP
b	Inner width of FRP
f_y	Steel tube yield strength
t_s	Steel tube thickness
σ_i	Tensile strength
E_s	Elastic modulus of steel
f_{sy}	Yield strength of steel
ε_{sy}	Yield strain of steel
μ	Poisson's ratio
H	Height of column
$S4R$	4-node shell elements
$C3D8R$	8-node brick element
$2a/2b$	Outer steel tube sides
X_N	Normalised parameter value
R^2	Coefficient of determination
$RMSE$	Root mean square error
MAE	Mean absolute error
BF	Basis function
$MARS$	Multivariate adaptive regression splines
$LS-SVM$	Least square-support vector machine
SVM	Support vector machine
$LSTM$	Long short-term memory
$BI-LSTM$	Bidirectional LSTM

1. Introduction

In structural engineering, innovation constantly drives advancements in building components to enhance efficiency. Fibre-reinforced polymer (FRP) composites have notably transformed civil engineering by offering a strong alternative to conventional materials [1,2]. Their exceptional strength-to-weight ratio and resistance to corrosion have garnered significant interest [3–6]. Combining FRP composites with traditional materials has given rise to hybrid structures, leveraging the strengths of both domains [7–10]. External confinements through FRP jackets have remarkably increased the strength and ductility of reinforced concrete columns [11–14].

Innovation extends to hybrid structures like FRP-concrete-steel double-skin tubular columns (DSTCs) and concrete-filled FRP tubes (CFFTs). These structures integrate an internal steel tube, an intermediary concrete layer, and an external FRP tube to optimise performance [15,16]. Extensive experimental studies have been conducted around the world to ascertain the behaviour of DSTCs [17,18]. These columns have demonstrated exceptional corrosion resistance and energy dissipation during seismic events [19]. However, prior research has predominantly focused on analysing single steel tubes [20,21], with only a scarce number of studies exploring the use of double steel tubes. Therefore, there is a pressing need for a comprehensive examination of the behaviour of double steel tubes filled with concrete and subjected to confinement by FRP composites. This exploration aims to delve into the interaction between the double steel tubes and the concrete infill, offering a novel perspective on its structural behaviour.

Integrating conventional analysis methods with advanced methodologies, the fusion of finite element model (FEM) and machine learning (ML) techniques has garnered significant attention in structural engineering. These tools are poised to revolutionise the predictive capabilities for structural forces and reactions [22,23]. FEM simulations offer insightful analyses across various structural scenarios, including complex configurations like FRP-constrained structures and seismic-resilient constructs [24–26]. Meanwhile, ML techniques, driven by data-driven learning models, enable computational systems to predict and decide without explicit programming. The synergy between ML and FEM promises precision and depth in understanding complex structural

behaviours [27], advancing predictive prowess in structural engineering by revealing hidden patterns within vast structural data.

This study highlights a comprehensive exploration of glass fibre-reinforced polymer (GFRP) and aramid fibre-reinforced polymer (AFRP) confined circular double-skin hollow tubular (DSHT) and double-skin double-filled tubular (DSDFT) columns. Employing FEM simulations through ABAQUS software, combined with ML techniques, the study delves into the structural performance of these columns (Fig. 1). The rigorous comparative analysis between DSHT and DSDFT columns, facilitated by 48 ABAQUS-modelled specimens, forms the crux of the research approach. Four distinct ML algorithms are evaluated to discern the optimal algorithm for predicting structural responses. The accuracy of results from the FEM simulations is confirmed through validation against prior experimental findings [28–30]. A systematic parametric study explores the influence of the introduction of double steel tubes, the diameter of the steel tube used, the type of FRP used, and the thickness of the FRP layer. A flowchart of the integrated process is highlighted in Fig. 2. This exhaustive investigation enriches the understanding of GFRP and AFRP confined circular single and double steel tube columns, ushering in new dimensions through the integration of ML techniques in response prediction. The findings extend the knowledge horizon and hold the potential to inform future design and analysis methodologies within the domain of structural engineering.

2. Methodology

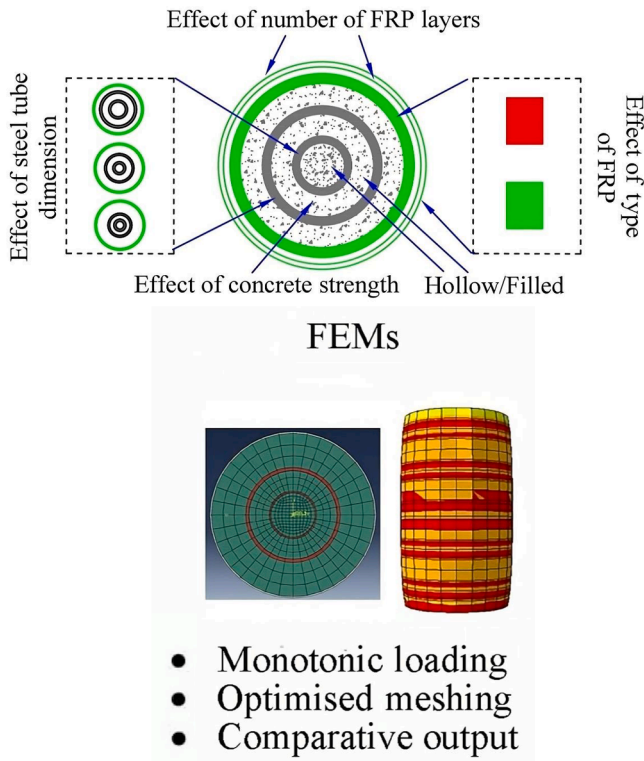
The methodology utilised in this investigation can be segmented into two primary components. The initial component involves the use of FEM to simulate the behaviour of DSHT and DSDFT columns, executed through the ABAQUS software. The subsequent phase centres on the integration of ML algorithms to predict axial loads and axial strains within DSHT and DSDFT columns. Detailed discussions regarding both methodologies are provided in the subsequent sections.

2.1. Finite element modelling

2.1.1. Development of FEMs

FEMs representing the DSHT and DSDFT circular columns are created within the computational environment of the ABAQUS software. These columns are characterised by a fixed height (H) of 305 mm and an outer diameter of 152.5 mm. In both configurations, namely DSHT and DSDFT, a layered composition is observed, beginning with an external layer made of GFRP or AFRP, succeeded by a layer of concrete. Moreover, in the case of DSHT columns, there exists an inner steel tube. On the other hand, for DSDFT columns, apart from the steel tube, there is an extra concrete layer followed by another inner steel tube. This inner steel tube has a diameter half the size of the previous one and is completed with concrete filling. It is important to highlight that the DSHT columns have an empty interior, while the DSDFT columns contain a core filled with concrete. These column configurations are visually represented in Fig. 3.

In this study, unidirectional GFRP and AFRP with a nominal thickness of 0.2 mm were employed. The material behaviour of GFRP and AFRP utilised in this investigation is modelled as orthotropic linear elastic before the point of tensile rupture. Unconfined concrete under uniaxial monotonic loading typically demonstrates brittle behaviour upon reaching its ultimate strength. The use of confinement, such as steel tubes or FRP, enhances the concrete's behaviour, enabling it to exhibit characteristics of inelastic (elastic-plastic) materials [31]. Confined concrete's strength and ductility primarily hinge upon the extent of lateral reinforcement-based confinement [31]. The core concrete enclosed within FRP experiences confinement pressure, which leads to lateral expansion of concrete as axial load intensifies – a phenomenon termed passive interaction. Within finite element analysis, accurately modelling concrete's stress-strain ($\sigma - \varepsilon$) relationship by incorporating this confinement pressure significantly contributes to the



AI generative model

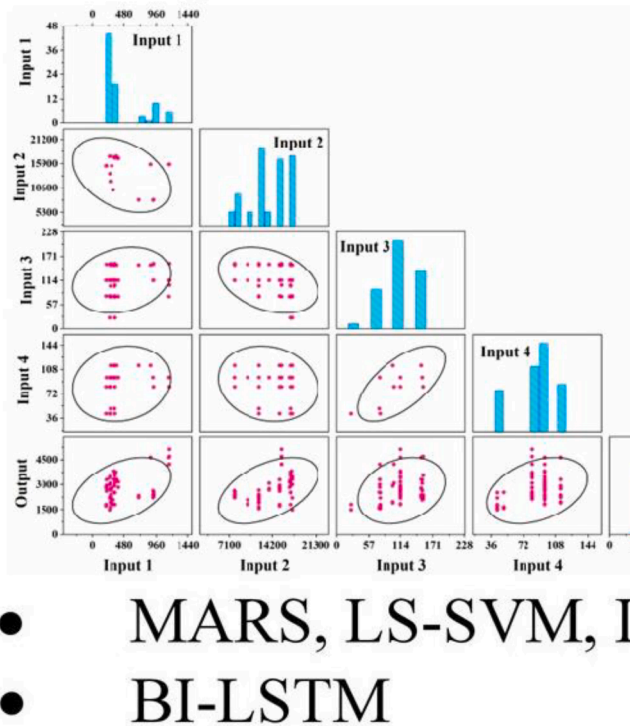


Fig. 1. Workflow of FEM and ML.

precision of the analysis result.

In the past, multiple researchers have put forward different models concerning concrete's behaviour, including the smeared cracking model (SCM), concrete damaged plastic model (CDPM), Drucker–Prager model (DPM), and brittle crack model (BCM). In this study, to simulate the

inelastic behaviour of concrete, CDPM is employed. By considering crushing and cracking of concrete, this model can depict the intricate character of the material. As a result, it is widely acknowledged while modelling the nonlinearity of concrete [32–34]. CDPM integrates various concrete properties like the compressive, tensile, plastic, and damaging behaviours. The Young's modulus value was derived from Eq. (1) [35], and a Poisson's ratio of 0.2 [36] was utilised. The density for normal-weight concrete was considered as 2400 kg/m³. The stress-strain curve of concrete is presented in Fig. 4.

$$E_c = 3320\sqrt{f'_c} + 6900 \quad (\text{Eq. (1)})$$

where f'_c is the compressive stress of the concrete material tested at 28 days.

According to the ABAQUS user manual [37], five concrete parameters are taken into account when analysing the plastic behaviour of concrete: dilation angle (ψ), viscosity parameter (μ_v), eccentricity (e), ratio of biaxial to uniaxial stresses (f_{bo}/f'_c), and yielding surface shape factor (K_c) [38]. All these elements were calibrated to attain the best possible alignment with the test measurement values which is listed in Table 1. An extensive analysis was provided by Isleem et al. [39] for a fuller understanding and the mathematics involved.

To accurately replicate the interaction between the FRP layers and concrete, tie constraints are employed, with the FRP layer assuming the role of the primary surface. Further, the steel tubes within concrete experience surface-to-surface contact using the penalty contact method, wherein a friction coefficient of 0.6 is implemented. Notably, in this context, the steel tube functions as the master surface.

The steel material is represented through solid elements following the $\sigma - \epsilon$ relation proposed by Tao et al. [40]. It is considered to have linear elastic behaviour with a density of 7.85×10^9 ton/mm³, Poisson's ratio of 0.25, and the elastic modulus as displayed in Table 2.

The FRP layers are modelled, and their stiffness is tailored through the incorporation of a reduction factor (R), contingent on the confinement stiffness ratio, and the aspect ratio of the columns. This R bears an inverse relationship with the confinement stiffness ratio and aspect ratio, aptly accounting for the behaviour of the FRP layers. The concrete types ranging from normal strength concrete to high strength concrete, characterised by compressive strengths of 42.5 MPa, 49.8 MPa, 82.4 MPa, 96.2 MPa, and 113.8 MPa are used.

The intricate interactions among FRP, concrete, and steel layers are conducted by employing suitable modelling methodologies and mathematical formulations, carefully considering the distinctive material properties, and prevailing failure criteria. Comprehensive details pertaining to the material properties for different diameters of steel tubes, GFRP, AFRP, and their relevant parameters are documented in Table 2.

2.1.2. Loading and boundary conditions

The loading and boundary conditions imposed on the column models play a crucial role in accurately simulating the axial behaviour of the specimens. The column configurations were exclusively subjected to axial loading to replicate realistic conditions accurately. To maintain homogeneity within the composite specimens during the loading process, the boundaries are carefully defined, and the interactions are given, as explained in Section 2.1.1.

A pivotal strategy of using the kinematic coupling mechanism is applied. The kinematic coupling establishes a connection between the steel tube, GFRP, and concrete layers at both ends of the columns. This coupling strategy facilitates the seamless transfer of displacements and rotations among the layers, thereby preserving their structural integrity throughout the loading regime. Specific reference points are strategically established within the model, as illustrated in Fig. 5(d) and (e). These reference points serve as anchors for the coupling connections between the distinct material layers. At these points, axial displacements and loads are precisely prescribed, ensuring an accurate simulation of the loading conditions.

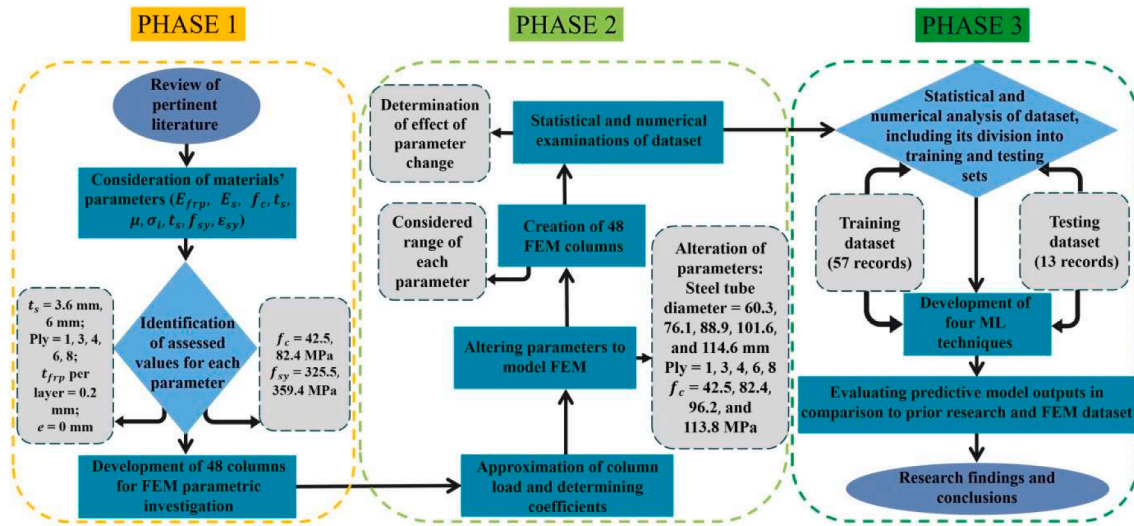


Fig. 2. Integrated process of FEM and ML.

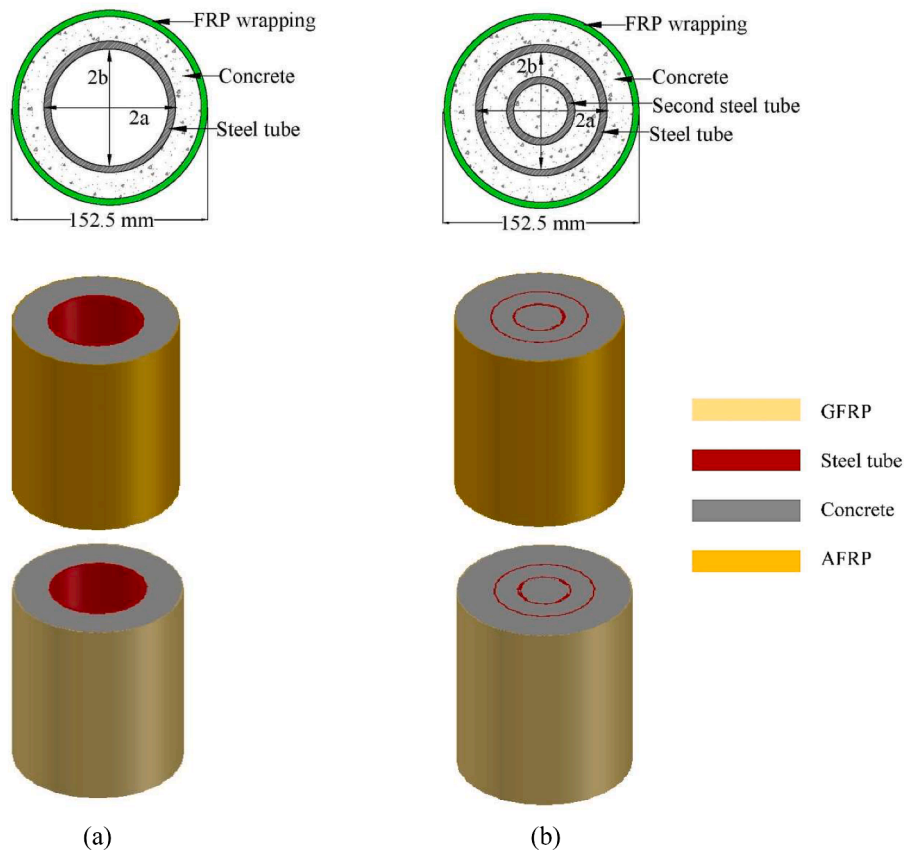


Fig. 3. Cross-sectional view of: (a) DSHT column and (b) DSDFT column.

Now, boundary conditions are enforced both at the upper and lower ends of the columns. The lower end is fixed against any rotation or movement in all three axes: X, Y, and Z, as depicted in Fig. 5(g). Conversely, the upper end is constrained from rotation and movement solely in the X and Y directions, while allowing freedom of movement along the Z-axis, as shown in Fig. 5(h). In the Z-direction, an axial displacement of 25 mm is induced to apply the axial compression load. This load is meticulously chosen to replicate practical loading scenarios, ensuring precise capture of the structural response. The adopted modelling strategy ensures the stability of the composite specimens

during the loading sequence, effectively mitigating any undesired lateral or rotational movements.

2.1.3. Meshing, element types, and analysis

The discretisation of the column models is a critical endeavour aimed at achieving an accurate representation of their geometry while effectively capturing the intricate behaviours of the composite materials during the axial loading. The analysis is performed utilising ABAQUS/explicit solver, renowned for its robust capabilities in dynamic simulations. To ensure computational efficiency and numerical stability, the

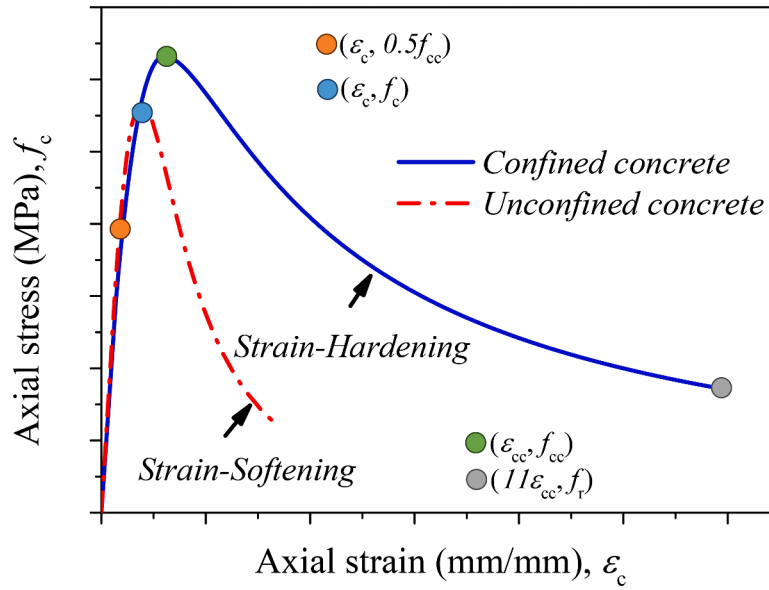


Fig. 4. Stress-strain curve for both uniaxially confined and unconfined concrete.

Table 1
Plasticity parameters of concrete for CDPM.

ψ	K_c	e	f_{bo}/f_c	μ_v
27°	0.667	0.1	1.16	0.0005

Table 2
Tensile properties of different steel tubes, GFRP, and AFRP.

Material	Outer diameter of steel tube (mm)	Thickness (mm)	Elastic modulus (MPa)	Yield stress (MPa)	Peak stress (MPa)	Axial peak strain (%)
Steel						
T ₁ ¹	60.300	3.60	203800	325.5	386.2	3.34
T ₂ ¹	76.100	3.20	200600	359.4	432.5	2.34
T ₃ ¹	88.900	3.20	199800	334.3	415.2	2.43
T ₄ ¹	101.60	3.20	198700	318.3	385.4	2.09
T ₅ ¹	114.60	6.00	201400	446.4	510.3	3.10
T ₆ ¹	114.30	6.02	200600	342.3	419.0	2.93
T ₃ ²	88.900	3.20	200000	314.2	387.9	2.02
T ₁ ²	60.300	3.60	200000	459.4	526.4	2.85
T ₁ ³	60.300	3.60	200000	319.0	384.0	3.34
T ₃ ²	88.900	3.20	200000	320.0	404.0	2.43
T ₆ ²	114.30	6.02	200000	449.0	524.0	3.10
FRP						
Glass	-	0.2	95300	-	3055	3.21
Aramid	-	0.2	128500	-	2390	1.86

central difference integration scheme is employed, which is recognised for its accuracy and stability. This integration scheme relies on small time increments to approximate the structural response, ensuring that the analysis output is based on the stable known parameters from the preceding time step. This approach effectively captures the time-dependent behaviours inherent to the column models. To enhance computational efficiency, a mass scaling technique is initiated at the outset of the analysis step, incorporating a scaling factor of 10. This technique optimally balances the kinetic and internal energy components within the model, thereby diminishing computational requirements without compromising the accuracy of the results. Moreover, step smoothing is introduced to minimise the velocities within the model, leading to reduced levels of kinetic energy. This

strategy, in turn, enables the analysis to focus on capturing the static response of the column models under the axial loading. The kinetic energy encompassing the entire model (ALLKE) is judiciously restricted to approximately 5 % of the total internal energy (ALLIE), in accordance with established recommendations for static analyses.

For the purpose of discretising the column models within the ABAQUS software environment, pertinent element types are judiciously selected, accounting for the material properties and the structural attributes of the constituent components.

The composite layers of FRP and steel tubes are modelled using specialised four-node shell elements (S4R), adept at representing thin-walled structures. These elements accurately capture the bending and membrane behaviours specific to the FRP's anisotropic properties while reducing computational costs compared to the solid elements. Concrete layers are simulated with solid homogeneous hexahedral elements (C3D8R) that efficiently handle compression and confinement responses, accounting for nonlinear material behaviours, stress distributions, and deformation characteristics. To maintain computational efficiency and coherence, a uniform mesh size of 25 mm is utilised for concrete elements in the column models. The key characteristics applied to FEMs are exhibited in Table 3. By eschewing substantial mesh size variations, a consistent and dependable analysis outcome is realised, engendering a high level of confidence in the acquired results.

The mesh configuration of the column models, elucidating the discretisation of concrete, steel tube, and FRP layers, is illustrated in Fig. 5. Comprehensive details regarding the modelled DSHT and DSDFT specimens are elaborated in Table 4.

2.2. ML methodology

The methodology adopted for this study involves the fusion of FEM simulations and ML techniques, with the primary objective of scrutinizing and predicting the behaviour of DSHT and DSDFT circular columns. The ensuing subsections present the procedures entailing data pre-processing, exploratory data analysis, and examination of four distinct ML algorithms.

2.2.1. Data pre-processing and normalisation

The dataset consists of 82 entries wherein the input parameters encompass: the product of the steel tube's cross-sectional area and its yield strength (GPa), the cross-sectional area of the column excluding both the hollow core and steel tubes, the number of FRP layers, and the

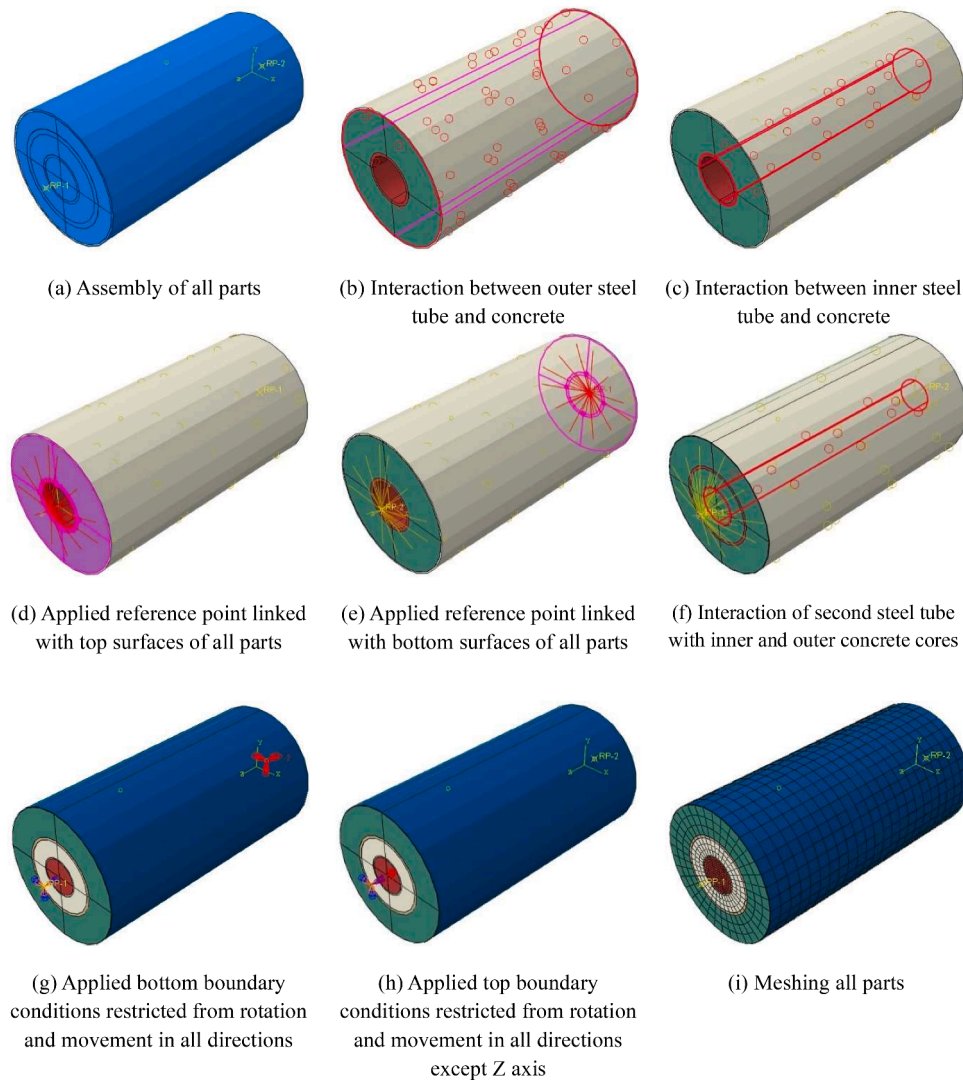


Fig. 5. Modelling DSHT and DSDFT columns.

Table 3
Properties of FEMs.

Property	Value
Mesh size of concrete material (mm)	15/ Element shape: Hex-structured
Mesh size of FRP tube (mm)	18/ Element shape: Quad-dominated, Free-advancing front
Mesh size of steel tube (mm)	13/ Element shape: Hex-structured
Minimum step size	1×10^{-8}
Initial step size	0.01
Maximum step size	1
Concrete and steel tube element type	Standard C3D8R/Geometric order: Linear/Family: 3D stress
FRP element type	Standard S4R/Geometric order: Linear/Family: 2D shell
Interaction constraint of FRP tube to concrete	Tie constraint/Surface to surface/Friction coefficient: 0.6
Applied displacement (mm)	25
Step-1 type	Static, General
Equation solver	Direct
Automatic stabilisation	Use damping factors from previous general steps

elastic modulus of FRP (GPa), and the concrete strength (MPa). These parameters are denoted as Input 1, Input 2, Input 3, and Input 4, respectively. Correspondingly, the output parameter, designated as

load-carrying capacity (kN), is labelled as output. Descriptive statistics pertaining to the dataset are indicated in Table 5, revealing a diverse range within the experimental data. It is evident that distinct columns demonstrate disparate distributions. To discern the relationships between the variable pairs, a pair-plot is shown in Fig. 6. Employing the Pearson correlation coefficient, a statistical analysis is conducted to ascertain the degree of correlation (DOC) between the input and output parameters, as depicted in Fig. 6. It can be observed from Fig. 7 that Input 1 ($r = 0.43$) and Input 2 ($r = 0.49$) manifest a stronger positive correlation with the output in comparison to Input 3 ($r = 0.26$) and Input 4 ($r = 0.36$).

To enhance the model's accuracy by mitigating associated errors, a min-max normalisation technique is employed to standardise the input and output parameters. This normalisation is executed via the following mathematical Eq. (2):

$$X_N = \frac{X - X_{\min}}{X_{\max} - X_{\min}} \quad (\text{Eq. (2)})$$

where X_N signifies the normalised parameter value, X represents the original parameter value, and X_{\min} and X_{\max} denote the minimum and maximum values within the input and output dataset, respectively.

2.2.2. Details of performance indices

Four distinct performance metrics are computed to assess the

Table 4
Details of modelled DSHT and DSDFT specimens.

Type	Specimen	Filling	Number of steel tube	FRP tube					Outer steel tube sides (mm)		Concrete strength (MPa)
				Type	Ply	t_{frp} (mm)	E_{frp} (MPa)	Tensile strength (MPa)	2a	2b	
DSHT	6G-H-S-T ₁ ¹	Hollow	Single	GFRP	6	1.2	95300	3055	60.3	53.1	96.2
DSDFT	6G-F-D-T ₁ ¹	Filled	Double	GFRP	6	1.2	95300	3055	60.3	53.1	96.2
DSDFT	4G-F-D-T ₁ ¹	Filled	Double	GFRP	4	0.8	95300	3055	60.3	53.1	96.2
DSHT	8G-H-S-T ₁ ¹	Hollow	Single	GFRP	8	1.6	95300	3055	60.3	53.1	96.2
DSHT	6G-H-S-T ₂ ¹	Hollow	Single	GFRP	6	1.2	95300	3055	76.1	69.7	96.2
DSDFT	6G-F-D-T ₂ ¹	Filled	Double	GFRP	6	1.2	95300	3055	76.1	69.7	96.2
DSDFT	4G-F-D-T ₂ ¹	Filled	Double	GFRP	4	0.8	95300	3055	76.1	69.7	96.2
DSHT	8G-H-S-T ₂ ¹	Hollow	Single	GFRP	8	1.6	95300	3055	76.1	69.7	96.2
DSHT	6G-H-S-T ₃ ¹	Hollow	Single	GFRP	6	1.2	95300	3055	88.9	82.5	96.2
DSDFT	6G-F-D-T ₃ ¹	Filled	Double	GFRP	6	1.2	95300	3055	88.9	82.5	96.2
DSDFT	4G-F-D-T ₃ ¹	Filled	Double	GFRP	4	0.8	95300	3055	88.9	82.5	96.2
DSHT	8G-H-S-T ₃ ¹	Hollow	Single	GFRP	8	1.6	95300	3055	88.9	82.5	96.2
DSHT	6G-H-S-T ₄ ¹	Hollow	Single	GFRP	6	1.2	95300	3055	101.6	95.2	96.2
DSDFT	6G-F-D-T ₄ ¹	Filled	Double	GFRP	6	1.2	95300	3055	101.6	95.2	96.2
DSDFT	4G-F-D-T ₄ ¹	Filled	Double	GFRP	4	0.8	95300	3055	101.6	95.2	96.2
DSHT	8G-H-S-T ₄ ¹	Hollow	Single	GFRP	8	1.6	95300	3055	101.6	95.2	96.2
DSHT	6G-H-S-T ₅ ¹	Hollow	Single	GFRP	6	1.2	95300	3055	114.6	102.6	96.2
DSDFT	6G-F-D-T ₅ ¹	Filled	Double	GFRP	6	1.2	95300	3055	114.6	102.6	96.2
DSDFT	4G-F-D-T ₅ ¹	Filled	Double	GFRP	4	0.8	95300	3055	114.6	102.6	96.2
DSHT	8G-H-S-T ₅ ¹	Hollow	Single	GFRP	8	1.6	95300	3055	114.6	102.6	96.2
DSHT	4A-H-S-T ₃ ²	Hollow	Single	AFRP	4	0.8	125700	2663	88.9	82.5	113.8
DSDFT	4A-F-D-T ₃ ²	Filled	Double	AFRP	4	0.8	125700	2663	88.9	82.5	113.8
DSHT	6A-H-S-T ₃ ²	Hollow	Single	AFRP	6	1.2	125700	2663	88.9	82.5	113.8
DSDFT	6A-F-D-T ₃ ²	Filled	Double	AFRP	6	1.2	125700	2663	88.9	82.5	113.8
DSHT	3A-H-S-T ₃ ²	Hollow	Single	AFRP	3	0.6	125700	2663	88.9	82.5	49.8
DSDFT	3A-F-D-T ₃ ²	Filled	Double	AFRP	3	0.6	125700	2663	88.9	82.5	49.8
DSHT	6A-H-S-T ₁ ²	Hollow	Single	AFRP	6	1.2	125700	2663	60.3	53.1	113.8
DSDFT	6A-F-D-T ₁ ²	Filled	Double	AFRP	6	1.2	125700	2663	60.3	53.1	113.8
DSHT	6A-H-S-T ₆ ¹	Hollow	Single	AFRP	6	1.2	125700	2663	114.3	102.26	113.8
DSDFT	6A-F-D-T ₆ ¹	Filled	Double	AFRP	6	1.2	125700	2663	114.3	102.26	113.8
DSHT	3A-H-S-T ₃ ³	Hollow	Single	AFRP	3	0.6	128500	2390	60.3	53.1	42.5
DSDFT	3A-F-D-T ₃ ³	Filled	Double	AFRP	3	0.6	128500	2390	60.3	53.1	42.5
DSDFT	1A-F-D-T ₃ ³	Filled	Double	AFRP	1	0.2	128500	2390	60.3	53.1	42.5
DSHT	3A-H-S-T ₃ ²	Hollow	Single	AFRP	3	0.6	128500	2390	88.9	82.5	42.5
DSDFT	3A-F-D-T ₃ ²	Filled	Double	AFRP	3	0.6	128500	2390	88.9	82.5	42.5
DSDFT	1A-F-D-T ₃ ²	Filled	Double	AFRP	1	0.2	128500	2390	88.9	82.5	42.5
DSHT	6A-H-S-T ₃ ²	Hollow	Single	AFRP	6	1.2	128500	2390	88.9	82.5	82.4
DSDFT	6A-F-D-T ₃ ²	Filled	Double	AFRP	6	1.2	128500	2390	88.9	82.5	82.4
DSDFT	4A-F-D-T ₃ ²	Filled	Double	AFRP	4	0.8	128500	2390	88.9	82.5	82.4
DSHT	6A-H-S-T ₆ ²	Hollow	Single	AFRP	6	1.2	128500	2390	114.3	102.26	82.4
DSDFT	6A-F-D-T ₆ ²	Filled	Double	AFRP	6	1.2	128500	2390	114.3	102.26	82.4
DSDFT	4A-F-D-T ₆ ²	Filled	Double	AFRP	4	0.8	128500	2390	114.3	102.26	82.4
DSHT	6G-H-S-T ₁ ³	Hollow	Single	GFRP	6	1.2	95300	3055	60.3	53.1	82.4
DSDFT	6G-F-D-T ₃ ³	Filled	Double	GFRP	6	1.2	95300	3055	60.3	53.1	82.4
DSHT	6G-H-S-T ₃ ²	Hollow	Single	GFRP	6	1.2	95300	3055	88.9	82.5	82.4
DSDFT	6G-F-D-T ₃ ²	Filled	Double	GFRP	6	1.2	95300	3055	88.9	82.5	82.4
DSHT	6G-H-S-T ₆ ²	Hollow	Single	GFRP	6	1.2	95300	3055	114.3	102.26	82.4
DSDFT	6G-F-D-T ₆ ²	Filled	Double	GFRP	6	1.2	95300	3055	114.3	102.26	82.4

Table 5
Descriptive statistics of input and output parameters.

Parameter	Mean	Standard error	Median	Standard deviation	Minimum	Maximum	Skewness	Kurtosis
Input 1	436.439	32.11917	291.423	290.8515	204.6449	1149.809	1.419556	0.44773
Input 2	13476.2	357.2383	13722.5	3234.931	7953.856	17470.87	-0.40643	-1.0641
Input 3	114.933	3.406904	114.36	30.85083	25.7	154.2	-0.47474	0.01566
Input 4	87.1195	2.448913	96.2	22.17585	42.5	113.8	-0.89605	-0.0512
Output	2641.80	87.33697	2418.04	790.8699	1480.27	5126.92	1.035888	1.03914

efficacy of the employed models [41,42]. Table 6 elucidates the optimal values and parametric equations corresponding to these metrics. For an impeccable prediction model, the values of these metrics must align precisely with their respective ideal values. The different ML models are

discussed in the following subsections.

2.2.3. Multivariate adaptive regression splines

The multivariate adaptive regression splines (MARS) technique, a

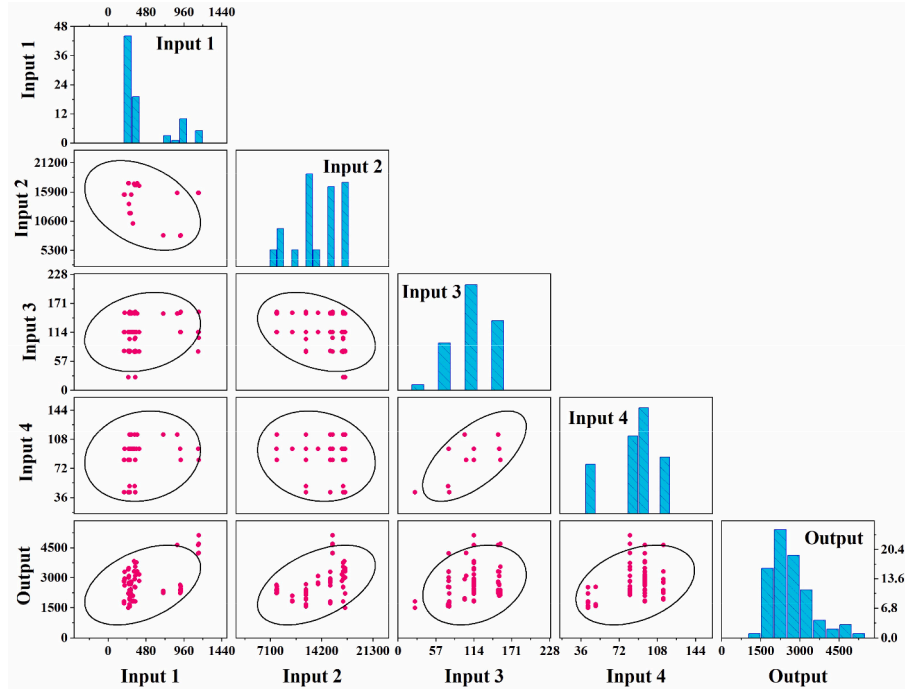


Fig. 6. Scatter matrix and pair-plot of input and output parameters.

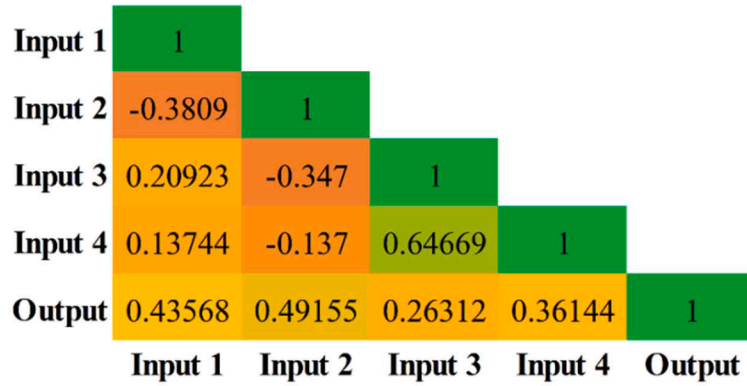


Fig. 7. Correlation matrix of input and output parameters.

Table 6

Performance metrics equations and their ideal values.

No.	Parameter	Equation	Ideal value
1	Coefficient of determination (R^2)	$R^2 = \frac{\sum_{i=1}^n (y_i - y_{mean})^2 - \sum_{i=1}^n (y_i - \hat{y}_i)^2}{\sum_{i=1}^n (y_i - y_{mean})^2}$ <p>y_i and \hat{y}_i are actual and predicted i^{th} values</p>	1
2	Adjusted coefficient of determination ($adj.R^2$)	$adj.R^2 = 1 - \frac{(n-1)}{(n-p-1)}(1 - R^2)$ <p>where p is number of input parameters</p>	1
3	Root mean square error (RMSE)	$RMSE = \sqrt{\frac{1}{N} \sum_{i=1}^n (y_i - \hat{y}_i)^2}$ <p>N is number of data sample</p>	0
4	Mean absolute error (MAE)	$MAE = \frac{1}{n} \sum_{i=1}^n (\hat{y}_i - y_i) $	0

nonparametric statistical approach, adeptly handles high-dimensional data. Through piecewise segments or splines, MARS captures intricate interactions between the input and dependent variables [43]. This yields continuous models with derivatives, distinct from recursive partitioning outcomes. MARS deduces relationships devoid of presupposed functional connections, utilising coefficients and basis functions determined by the dataset. A cornerstone is the spline function, underpinning basis functions with piecewise linear segments. These segments, termed splines, partition data effectively. By merging polynomial segments at specific locations (knots), the MARS model introduces basis functions, enhancing the capacity to capture nonlinearities. The MARS model iteratively generates basis functions by exhaustively exploring univariate knots and potential variable interactions. The model's generalisability improves through backward steps that prune the less impactful terms, curbing overfitting [44]. The MARS model response, $f(x)$, comprises basis functions and interactions. Here, in Eq. (3) $BF(x)$ signifies a spline basis function, while β_0 and β_n represent intercept and n^{th} BF coefficients, respectively, with N total basis functions.

$$f(x) = \beta_0 + \sum_{n=1}^N \beta_n BF(x) \quad (\text{Eq. (3)})$$

The MARS model is constructed using the MATLAB 2018a software. The initial prediction of the normalised output MARS model involved 15 basis functions. After the pruning phase, several basis functions were eliminated, leaving the five most effective basis functions as detailed in Table 7. Leveraging the correlation equation, Eq. (4) identified, the normalised output, namely load-carrying capacity, is subsequently determined.

$$\begin{aligned} \text{Output} = & 0.7172 + 1.0536 \times BF1 - 0.30944 \times BF2 + 1.1551 \times BF3 \\ & - 0.50747 \times BF4 - 1.0883 \times BF5 \end{aligned} \quad (\text{Eq. (4)})$$

2.2.3. Least square–support vector machine

Introduced by Vapnik [45], the least square–support vector machine (LS-SVM) method finds its roots in statistical learning theory, offering a solution for tackling local minimum and nonlinear challenges in high-dimensional spaces. This approach is an enhancement of the support vector machine (SVM) model and introduces two novel parameters. The conventional inequality constraints are substituted with equality constraints, effectively transforming the pair of programming problems into linear equations. Notably, these modifications contribute to a reduction in computation time in comparison to the SVM model. The LS-SVM framework defines the regression function linking Input (i) and Output (O) through Eq. (5), where α_i signifies the i^{th} Lagrange multiplier, K denotes the kernel function, and b represents the bias. Within this context, Eq. (6) indicates the application of the radial basis function (RBF) kernel function, pivotal in this study, where σ corresponds to a parameter influencing the algorithm's accuracy. The hyper-parameters selected for optimising the LS-SVM model's construction entail a cost parameter of 100 and a sparsity constraint of 10.

$$O = \alpha_1 k(i, i_1) + \alpha_2 k(i, i_2) + \dots + \alpha_n k(i, i_n) + b \quad (\text{Eq. (5)})$$

$$k(x, x_i) = \exp\left(\frac{-\|x - x_i\|^2}{2\sigma^2}\right) \quad (\text{Eq. (6)})$$

2.2.4. Long short-term memory

Long short-term memory (LSTM), a class of recurrent neural networks, stands out as an effective and scalable solution for addressing the diverse learning challenges inherent in sequential data. Its effectiveness and generality render it suitable for capturing temporal dependencies across the extended sequences [46]. Functioning as a specialised type of recurrent neural network, LSTM employs gated mechanisms to control information flow among its constituent neurons.

Through the orchestrated interplay between input and forget gates, a refined version of the cell state is generated, enriched by the contextual understanding of inputs [47]. Despite its virtues, the LSTM architecture has faced critique for its complexity and somewhat arbitrary features, some of whose functionalities remain unclear. This prompts a discourse over whether LSTM represents an optimal design choice or whether superior alternatives may exist. A schematic depiction of the foundational LSTM algorithm is displayed in Fig. 8. The current study determines the optimal hyper-parameters for the LSTM model construction as follows: hidden nodes = 70, activation function = sigmoid, epochs = 500, batch size = 12, optimiser = Adam, return sequence = true, and loss function = mean_squared_error.

Table 7
Equations for MARS model's basis functions.

No.	Basis function	Equation
1	BF1	$\max(0, x_1 - 0.75069)$
2	BF2	$\max(0, 0.7506 - x_1)$
3	BF3	$\max(0, x_2 - 0.95427)$
4	BF4	$\max(0, 0.95427 - x_2)$
5	BF5	$BF2 \times \max(0, 0.6899 - x_3)$

2.2.5. Bidirectional LSTM

The pioneering work of Schuster and Paliwal [49] introduced the bidirectional LSTM (BI-LSTM) model, designed to harness both the past and future input data sequences for training. This architecture employs two interconnected layers to process input data [50]. By leveraging the historical and prospective context of the elements, BI-LSTM undertakes the prediction or tagging of sequences, considering a limited sequence length. This outcome is achieved through the simultaneous operation of a left-to-right LSTM in conjunction with a right-to-left LSTM. The composite output constitutes the predicted value of a specific target signal, yielding remarkably favourable results. The architectural blueprint of BI-LSTM is illustrated in Fig. 9. Eqs. (7) and (8) serve to compute the forward function of BI-LSTM with L unit inputs and H hidden units. Notably, the BI-LSTM network stores two distinct values within its hidden layer. In forward and backward computations, both the matrix A and its transpose play a pivotal role. The ultimate value y is a product of both the matrix A and its transposed counterpart [51]:

$$\alpha'_h = \sum_{i=1}^L x'_i w_{ih} + \sum_{i=1}^H b'^{-1}_{ih} w_{ih} \quad (\text{Eq. (7)})$$

$$\alpha'_h = \theta_h(\alpha'_h) \quad (\text{Eq. (8)})$$

The current study identifies the optimal hyper-parameters for constructing the BI-LSTM model as follows: hidden nodes = 64, activation function = sigmoid, epochs = 500, batch size = 12, optimiser = Adam, return sequence = true, and loss function = mean_squared_error.

In the current investigation, the implementation of these four ML algorithms is adopted, and their respective performances have been meticulously examined. This comprehensive evaluation aims to discern the most effective approach for scrutinising and prognosticating the behaviour and performance of the DSHT and DSDFT columns. The overarching goal is to pinpoint the algorithm that delivers precise and dependable outcomes, instilling a heightened level of confidence in the resultant predictions.

3. Illustrations, validation, and discussion of FEMs

To ascertain the precision and dependability of FEMs formulated via the ABAQUS software, an exhaustive validation investigation is executed through a comparative analysis of simulation outcomes against experimental findings of three distinct scholarly works: Article 1 authored by Louk Fanggi and Ozbakkaloglu [28], Article 2 by Louk Fanggi and Ozbakkaloglu [29], and Article 3 by Albitar et al. [30]. This empirical inquiry encompasses the emulation of 48 circular columns, divided into two sets of 24 columns each: DSHT and DSDFT, all undergoing the axial compression. Amid these columns, 22 are sheathed with AFRP, while 26 are enveloped with GFRP. A gamut of ten steel tubes, distinguished by the diameter and material attributes as delineated in Table 2, is deployed. The height of each column is calibrated to 305 mm, in congruence with the experimental framework outlined in Articles 1, 2, and 3. Variance in concrete strength is accounted for, spanning five levels: 42.5 MPa, 49.8 MPa, 82.4 MPa, 96.2 MPa, and 113.8 MPa, ensuring parity between the experimental and numerical investigations.

The primary indices of performance for validation proceedings are the ultimate axial load and ultimate axial strain of the DSHT columns. The DSDFT columns mirror the initial DSHT configuration but introduce a novel structure: the hollow segment of DSHT columns is supplemented with an additional steel tube, possessing a diameter equivalent to 0.5 times that of the initial steel tube; the void within this secondary steel tube is then packed with concrete. The validation findings manifest a conspicuous congruence between FEMs and experimental observations. Prediction of the ultimate load-carrying capacity garnered from FEMs evinces close alignment with experimental results, exhibiting a maximum divergence of 12.14 % and a minimum disparity of 0.07 %. Correspondingly, predictions of the ultimate strain portray satisfactory

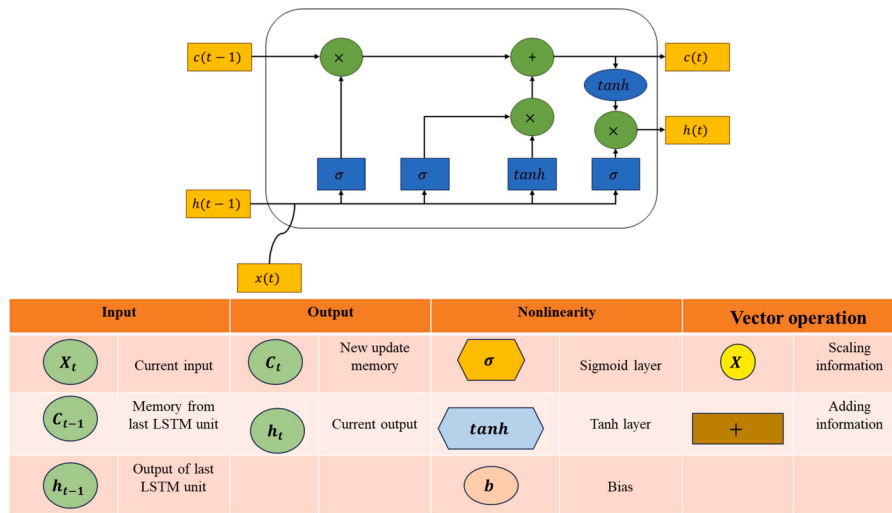


Fig. 8. Architecture of a LSTM algorithm [48].

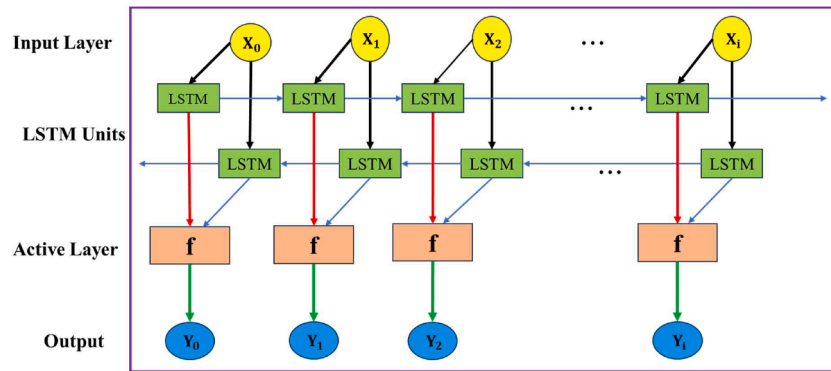


Fig. 9. Architecture of a BI-LSTM algorithm [48].

accord, marked by a maximum deviation of 24.02 % and a minimum deviation of 0.52 %. These minor discrepancies underscore the conservative tendency of FEMs, yielding values slightly surpassing experimental outcomes.

An elaborate comparative assessment, elucidated in Table 8 and Fig. 10, presents the computed deviations for each DSHT column, juxtaposing FEMs against experimental data in Articles 1, 2, and 3. Table 8 also furnishes data regarding the ultimate axial load and ultimate axial strain of the proposed DSDFT columns. The notable concurrence between the simulation outcomes and the experimental observations substantiates the precision and dependability of the formulated FEMs. This alignment affirms the capability of the developed FEMs to accurately depict the response of both DSHT and DSDFT columns under the influence of the axial compression. Further, an organised parametric exploration delves into the impact of factors including the incorporation of double steel tubes, dimensions of utilised steel tubes, variety of FRP materials engaged, and thickness of FRP layers using the different column models, as demonstrated in Table 8. Fig. 11 shows the strain and stress datasets extracted from FEMs for a subset of the chosen DSHT columns, alongside their corresponding DSDFT counterparts.

3.1. Effect of double steel tubes

The investigation into the effect of providing a double steel tube configuration on the behaviour of FRP (GFRP and AFRP) confined circular columns (DSHT vs. DSDFT) provides intriguing insights into the structural performance of these configurations. This section discusses

the findings related to the ultimate axial load and ultimate axial strain, focusing on the influence of the double steel tube arrangement.

From Table 9 and Figs. 12(a) and 13 it is deduced that there is a substantial increase in the ultimate axial load-carrying capacity in the DSDFT columns compared to the DSHT columns. For the initial steel tube diameter of 60.3 mm, the DSHT columns exhibited an ultimate axial load of 2903.98 kN, whereas the DSDFT columns gave a substantial increase to 3471.55 kN, reflecting a notable 19.54 % increment. This trend of enhanced load-carrying capacity continues across the varying steel tube diameters, with the percentage increase in the ultimate axial load displaying a consistent upward trajectory reaching up to 101.21 % for an initial steel tube diameter of 114.6 mm. It is also noted that as the initial steel tube diameter increases, the percentage increase in the ultimate axial load between the two configurations also escalates. This augmentation in the ultimate axial load is due to multiple factors.

Firstly, the presence of an additional inner steel tube and concrete fill in the DSDFT configuration, in contrast to the DSHT configuration, serves as supplementary material capable of bearing extra loads. This configuration effectively redistributes the load, thereby enhancing the overall load-carrying capacity of the column. Secondly, this added inner tube and concrete fill noticeably contribute to an improved confinement effect. This effect generates greater lateral support for the column, consequently increasing its load-carrying capacity. Thirdly, the multi-layered arrangement of the DSDFT columns provides a more robust structural integrity compared to the DSHT columns. This heightened integrity enables the column to better withstand the deformation and resist failure under the axial compression, thereby contributing to the observed increase in load-carrying capacity. Lastly, the additional

Table 8

Ultimate axial load and axial strain for DSHT and DSDFT columns.

Study	Type	Specimen	Experimental result		FEM result		Deviation (%)	
			Axial load (kN)	Axial strain (mm/mm)	Axial load (kN)	Axial strain (mm/mm)	Load	Strain
Article 1	DSHT	6G-H-S-T ₁ ¹	2940.00	0.0351	2903.98	0.0345	-1.23	-1.76
Article 1	DSHT	6G-H-S-T ₁ ¹	2608.00	0.0278	2903.98	0.0345	11.35	24.02
Present	DSDFT	6G-F-D-T ₁ ¹	-	-	3471.55	0.0356	-	-
Present	DSDFT	4G-F-D-T ₁ ¹	-	-	3007.73	0.0359	-	-
Present	DSHT	8G-H-S-T ₁ ¹	-	-	3290.76	0.0344	-	-
Article 1	DSHT	6G-H-S-T ₂ ¹	2741.00	0.0394	2720.82	0.0373	-0.74	-5.32
Article 1	DSHT	6G-H-S-T ₂ ¹	2668.00	0.0360	2720.82	0.0373	1.98	3.61
Present	DSDFT	6G-F-D-T ₂ ¹	-	-	3815.11	0.0396	-	-
Present	DSDFT	4G-F-D-T ₂ ¹	-	-	3303.90	0.0404	-	-
Present	DSHT	8G-H-S-T ₂ ¹	-	-	3076.69	0.0369	-	-
Article 1	DSHT	6G-H-S-T ₃ ¹	2212.00	0.0299	2396.09	0.0345	8.32	15.46
Article 1	DSHT	6G-H-S-T ₃ ¹	2352.00	0.0353	2396.09	0.0345	1.87	-2.19
Present	DSDFT	6G-F-D-T ₃ ¹	-	-	3757.88	0.0369	-	-
Present	DSDFT	4G-F-D-T ₃ ¹	-	-	3290.96	0.0378	-	-
Present	DSHT	8G-H-S-T ₃ ¹	-	-	2653.04	0.0334	-	-
Article 1	DSHT	6G-H-S-T ₄ ¹	1798.00	0.0250	1824.95	0.0307	1.50	22.92
Article 1	DSHT	6G-H-S-T ₄ ¹	1850.00	0.0303	1824.95	0.0307	-1.35	1.42
Present	DSDFT	6G-F-D-T ₄ ¹	-	-	3156.37	0.0310	-	-
Present	DSDFT	4G-F-D-T ₄ ¹	-	-	2836.69	0.0315	-	-
Present	DSHT	8G-H-S-T ₄ ¹	-	-	2086.21	0.0298	-	-
Article 1	DSHT	6G-H-S-T ₅ ¹	2367.00	0.0318	2338.36	0.0343	-1.21	7.99
Article 1	DSHT	6G-H-S-T ₅ ¹	2215.00	0.0277	2338.36	0.0343	5.57	23.97
Present	DSDFT	6G-F-D-T ₅ ¹	-	-	4643.45	0.0383	-	-
Present	DSDFT	4G-F-D-T ₅ ¹	-	-	4223.11	0.0392	-	-
Present	DSHT	8G-H-S-T ₅ ¹	-	-	2637.01	0.0332	-	-
Article 2	DSHT	4A-H-S-T ₃ ²	1919.00	0.0289	1907.36	0.0306	-0.61	5.88
Article 2	DSHT	4A-H-S-T ₃ ²	1965.00	0.0292	1907.36	0.0306	-2.93	4.79
Present	DSDFT	4A-F-D-T ₃ ²	-	-	2914.89	0.0325	-	-
Article 2	DSHT	6A-H-S-T ₃ ²	2247.00	0.0294	2242.33	0.0301	-0.21	2.38
Article 2	DSHT	6A-H-S-T ₃ ²	2251.00	0.0310	2242.33	0.0301	-0.38	-2.90
Present	DSDFT	6A-F-D-T ₃ ²	-	-	3300.33	0.0315	-	-
Article 2	DSHT	3A-H-S-T ₃ ²	1664.00	0.0422	1572.13	0.0401	-5.52	-5.01
Article 2	DSHT	3A-H-S-T ₃ ²	1567.00	0.0380	1572.13	0.0401	0.33	5.48
Present	DSDFT	3A-F-D-T ₃ ²	-	-	2534.11	0.0419	-	-
Article 2	DSHT	6A-H-S-T ₁ ²	2745.00	0.0241	2755.56	0.0257	0.38	6.49
Article 2	DSHT	6A-H-S-T ₁ ²	2783.00	0.0213	2755.56	0.0257	-0.99	20.49
Present	DSDFT	6A-F-D-T ₁ ²	-	-	3305.58	0.0254	-	-
Article 2	DSHT	6A-H-S-T ₆ ¹	2331.00	0.0333	2305.15	0.0319	-1.11	-4.13
Article 2	DSHT	6A-H-S-T ₆ ¹	2228.00	0.0311	2305.15	0.0319	3.46	2.65
Present	DSDFT	6A-F-D-T ₆ ¹	-	-	4638.30	0.0364	-	-
Article 3	DSHT	3A-H-S-T ₁ ³	1722.00	0.0367	1784.86	0.0403	3.65	9.83
Article 3	DSHT	3A-H-S-T ₁ ³	1802.00	0.0401	1784.86	0.0403	-0.95	0.52
Present	DSDFT	3A-F-D-T ₁ ³	-	-	2199.52	0.0411	-	-
Present	DSDFT	1A-F-D-T ₁ ³	-	-	1480.27	0.0426	-	-
Article 3	DSHT	3A-H-S-T ₃ ²	1587.00	0.0399	1555.09	0.0419	-2.01	4.94
Article 3	DSHT	3A-H-S-T ₃ ²	1553.00	0.0380	1555.09	0.0419	0.13	10.19
Present	DSDFT	3A-F-D-T ₃ ²	-	-	2523.00	0.0437	-	-
Present	DSDFT	1A-F-D-T ₃ ²	-	-	1799.95	0.0462	-	-
Article 3	DSHT	6A-H-S-T ₃ ²	2132.00	0.0296	2241.74	0.0281	5.15	-5.00
Article 3	DSHT	6A-H-S-T ₃ ²	2212.00	0.0293	2241.74	0.0281	1.34	-4.02
Present	DSDFT	6A-F-D-T ₃ ²	-	-	3542.73	0.0296	-	-
Present	DSDFT	4A-F-D-T ₃ ²	-	-	3086.35	0.0304	-	-
Article 3	DSHT	6A-H-S-T ₆ ²	2367.00	0.0368	2369.98	0.0356	0.13	-3.32
Article 3	DSHT	6A-H-S-T ₆ ²	2331.00	0.0346	2369.98	0.0356	1.67	2.82
Present	DSDFT	6A-F-D-T ₆ ²	-	-	4689.62	0.0398	-	-
Present	DSDFT	4A-F-D-T ₆ ²	-	-	4238.60	0.0407	-	-
Article 3	DSHT	6G-H-S-T ₁ ³	2799.00	0.0358	2835.94	0.0388	1.32	8.38
Article 3	DSHT	6G-H-S-T ₁ ³	2838.00	0.0350	2835.94	0.0388	-0.07	10.86
Present	DSDFT	6G-F-D-T ₁ ³	-	-	3409.12	0.0395	-	-
Article 3	DSHT	6G-H-S-T ₃ ²	2355.00	0.0450	2349.16	0.0390	-0.25	-13.33
Article 3	DSHT	6G-H-S-T ₃ ²	2182.00	0.0348	2349.16	0.0390	7.66	12.06
Present	DSDFT	6G-F-D-T ₃ ²	-	-	3732.27	0.0415	-	-
Article 3	DSHT	6G-H-S-T ₆ ²	2440.00	0.0455	2562.43	0.0435	5.02	-4.47
Article 3	DSHT	6G-H-S-T ₆ ²	2285.00	0.0378	2562.43	0.0435	12.14	14.98
Present	DSDFT	6G-F-D-T ₆ ²	-	-	5126.92	0.0493	-	-

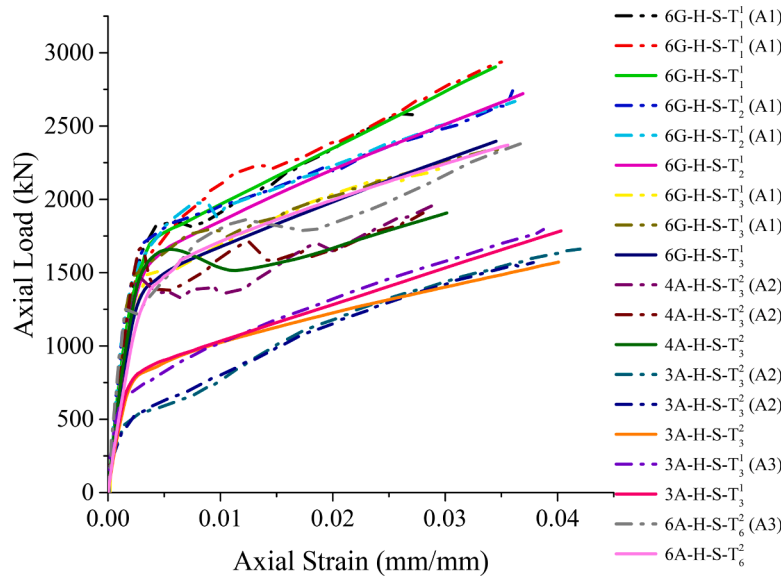


Fig. 10. Validation of FEMs with experimental models of Article 1 (A1), Article 2 (A2), and Article 3 (A3).

concrete layer within the DSDFT columns plays a pivotal role in enhancing the crack control and energy absorption during loading. This characteristic has led to a more ductile response, evident from Table 9, where the axial strain of the DSDFT columns surpasses that of the DSHT columns. With the steel tube diameter of 60.3 mm, the DSHT columns manifest an ultimate axial strain of 0.0345, while the DSDFT columns register an ultimate axial strain of 0.0356, representing a 3.18 % increase. The concrete core acts as a buffer that can absorb energy during the deformation, thereby allowing the column to sustain larger deformations without abrupt failure. This enhanced ductility allows the DSDFT columns to have a higher load-carrying capacity.

A similar trend is observed for AFRP confinement (Fig. 12(b) and Fig. 13) for both the ultimate axial load and ultimate axial strain. However, for a steel tube diameter of 60.3 mm and 6 AFRP confinement layers, the DSHT columns presented an ultimate axial strain of 0.0257, whereas the DSDFT columns illustrated a slightly lower strain of 0.0254, indicating a small decline of -1.16 %. This witnessed discrepancy, while contrary to the general trend observed across other parameters, appears to be within a negligible range and might be attributed to the computational refinement or numerical variations inherent in the simulation. However, this is not a universal trend, as evident from other cases where the DSDFT columns show higher strains.

3.2. Effect of FRP tube thickness

The thickness of FRP layers applied to the confined columns plays a pivotal role in shaping their structural performance. This section demonstrates the intriguing outcomes observed through the manipulation of the number of FRP layers in both the GFRP and AFRP confined columns.

Upon thorough examination of Table 10 and Figs. 14 and 15, a consistent trend emerges within both the GFRP and AFRP-confined DSHT and DSDFT columns. An increase in the thickness of FRP layers, each increment measuring 0.2 mm, accompanies a notable increase in the ultimate axial load while triggering a simultaneous decline in the ultimate axial strain. Noteworthy observations unfold particularly within the DSHT columns utilising GFRP, revealing a remarkable surge of 10 % to 14 % in the ultimate axial load-carrying capacity as layers progress from 6 to 8. Similarly, in the DSDFT columns, the transition from 4 to 6 layers elicited a substantial 10 % to 15 % increment in the load-carrying capacity. This observed behaviour resonates across AFRP confinement scenarios. In the context of the DSDFT columns, the progression from 1 to 3 layers yielded an impressive 40 % increase in the

ultimate axial load-carrying capacity, whereas within the DSHT columns, the increase was approximately 18 %. Similar results were obtained by Wong et al. [18], Ozbakkaloglu and Louk Fanggi [52] and Albitar et al. [30] where an increase in the thickness of FRP resulted in a corresponding increase in the ultimate axial load-carrying capacity of the columns. Increased thickness or additional layers of FRP result in the intensified confinement. This confinement leads to an enhanced lateral support to the confined concrete core, distributing the applied load more effectively. Consequently, the columns exhibit the increased load-carrying capacities as more layers contribute to reinforcing the structure against the axial compression.

Thicker layers also exhibit increased stiffness, but decreased elongation capabilities compared to thinner layers. As confinement increases with thicker FRP layers, the concrete core experiences greater lateral confinement pressure, limiting its ability to deform under the axial load. This restriction in the deformation translates into reduced the axial strain due to the enhanced stiffness of the structure. Within the AFRP-confined DSDFT columns, the shift from 1 to 3 layers leads to a reduction in the ultimate strain by 4 % to 5 %.

3.3. Effect of steel tube diameter

The diameter of the steel tube within confined columns exerts a significant influence on their structural behaviour and performance. As depicted in Table 2, the alteration in the diameter of the initial steel tube is accompanied by concurrent changes in the yield stress of the steel tube, the thickness of the steel tube, and the area of the confined concrete. As can be seen from Table 11, the DSHT and DSDFT columns with an outer steel tube diameter of 60.3 mm are compared against an outer steel tube diameter of 76.1 mm, 88.9 mm, 101.6 mm, and 114.6 mm. Figs. 16 and 17 illustrate graphically the effect of the steel tube diameter on the DSHT and DSDFT columns.

In the case of the DSHT columns, an intriguing consistency emerges: an increase in the outer steel tube diameter results in a decrement in the ultimate axial load-carrying capacity of the columns. This trend can be attributed to the fact that a larger diameter of the steel tube leads to lesser concrete being present between the sandwiched section of FRP and steel tube. This reduction in the area of concrete present in the column results in decrement of the load-carrying capacity of the columns. Notably, the ultimate axial load-carrying capacity of the DSHT columns decreases by approximately 37.16 % as the diameter of the steel tube increases from 60.3 mm to 101.6 mm.

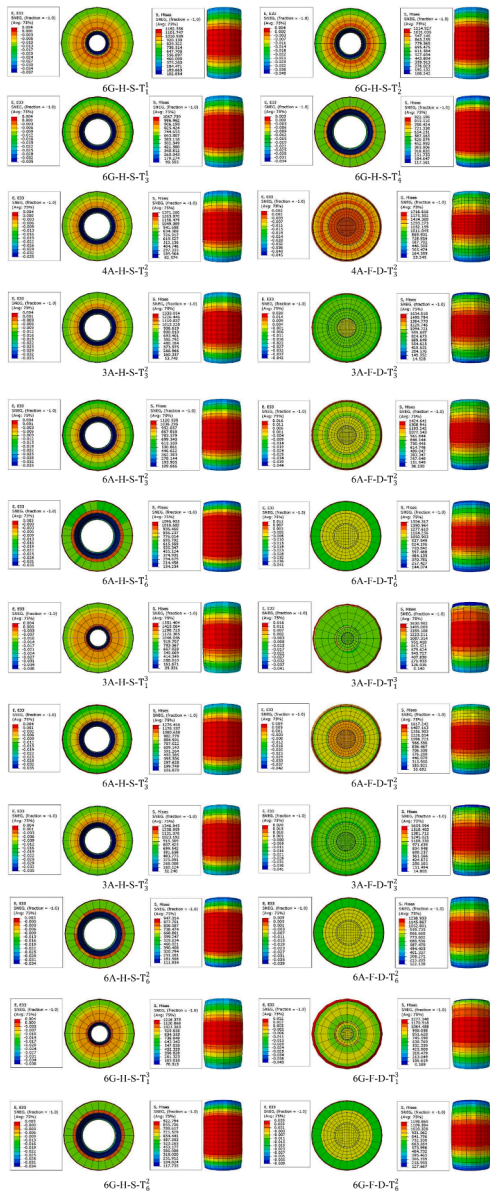


Fig. 11. Strain and stress data from ABAQUS models.

Contrasting to this trend, the behaviour exhibited by the DSDFT columns portrays a diametrically opposite scenario. Here, an increase in the outer steel tube diameter corresponds proportionately to an increase in both the ultimate axial load-carrying capacity and ultimate axial strain. As the outer steel tube diameter increases from 60.3 mm to 114.6 mm, the ultimate axial load-carrying capacity notably increases by 40.41 %, while the ultimate axial strain increases by 9.19 %. These findings remarkably align with prior research by Wong et al. [18], Ozbakkaloglu and Louk Fanggi [52], and Louk Fanggi and Ozbakkaloglu [29], validating the positive correlation between the diameter of the steel tube and the ultimate axial stress capacity of the confined concrete. However, for the outer steel tube diameter of 101.6 mm, it is observed that the ultimate load-carrying capacity of the column decreases by 20.64 % when compared to the column with an outer diameter of 60.3 mm which is in agreement with Louk Fanggi and Ozbakkaloglu [28] and Albitar et al. [30] where they found that the ultimate axial stress capacity of the confined concrete decreases with increase in the steel tube diameter. This marks that a split consensus within the existing literature regarding the precise influence of the steel tube diameter on the ultimate axial stress experienced by the confined concrete exists. This difference

Table 9

Comparison of axial load and axial strain of DSDFT and DSHT columns.

Specimen	Axial load (kN)	Increment (%)	Axial strain (mm/mm)	Increment (%)
6G-H-S-T ₁ ¹	2903.98	19.54	0.0345	3.18
6G-F-D-T ₁ ¹	3471.55		0.0356	
6G-H-S-T ₂ ¹	2720.82	40.21	0.0373	6.17
6G-F-D-T ₂ ¹	3815.11		0.0396	
6G-H-S-T ₃ ¹	2396.09	56.83	0.0345	6.95
6G-F-D-T ₃ ¹	3757.88		0.0369	
6G-H-S-T ₄ ¹	1824.95	72.95	0.0307	0.97
6G-F-D-T ₄ ¹	3156.37		0.0310	
6G-H-S-T ₅ ¹	2338.36	98.57	0.0343	11.66
6G-F-D-T ₅ ¹	4643.45		0.0383	
4A-H-S-T ₃ ²	1907.36	52.82	0.0306	6.21
4A-F-D-T ₃ ²	2914.89		0.0325	
6A-H-S-T ₃ ²	2242.33	47.18	0.0301	4.65
6A-F-D-T ₃ ²	3300.33		0.0315	
3A-H-S-T ₃ ²	1572.13	61.18	0.0401	4.48
3A-F-D-T ₃ ²	2534.11		0.0419	
6A-H-S-T ₂ ²	2755.56	19.96	0.0257	-1.16
6A-F-D-T ₂ ²	3305.58		0.0254	
6A-H-S-T ₆ ¹	2305.15	101.21	0.0319	14.10
6A-F-D-T ₆ ¹	4638.30		0.0364	
3A-H-S-T ₁ ³	1784.86	23.23	0.0403	1.98
3A-F-D-T ₁ ³	2199.52		0.0411	
3A-H-S-T ₃ ²	1555.09	62.24	0.0419	4.29
3A-F-D-T ₃ ²	2523.00		0.0437	
6A-H-S-T ₆ ²	2369.98	97.87	0.0356	11.79
6A-F-D-T ₆ ²	4689.62		0.0398	
6G-H-S-T ₁ ³	2835.94	20.21	0.0388	1.80
6G-F-D-T ₁ ³	3409.12		0.0395	
6G-H-S-T ₃ ²	2349.16	58.87	0.0390	6.41
6G-F-D-T ₃ ²	3732.27		0.0415	
6G-H-S-T ₆ ²	2562.43	100.08	0.0435	13.33
6G-F-D-T ₆ ²	5126.92		0.0493	

highlights the necessity for in-depth exclusive research concentrating specifically on the effects of the inner steel tube diameter in future studies.

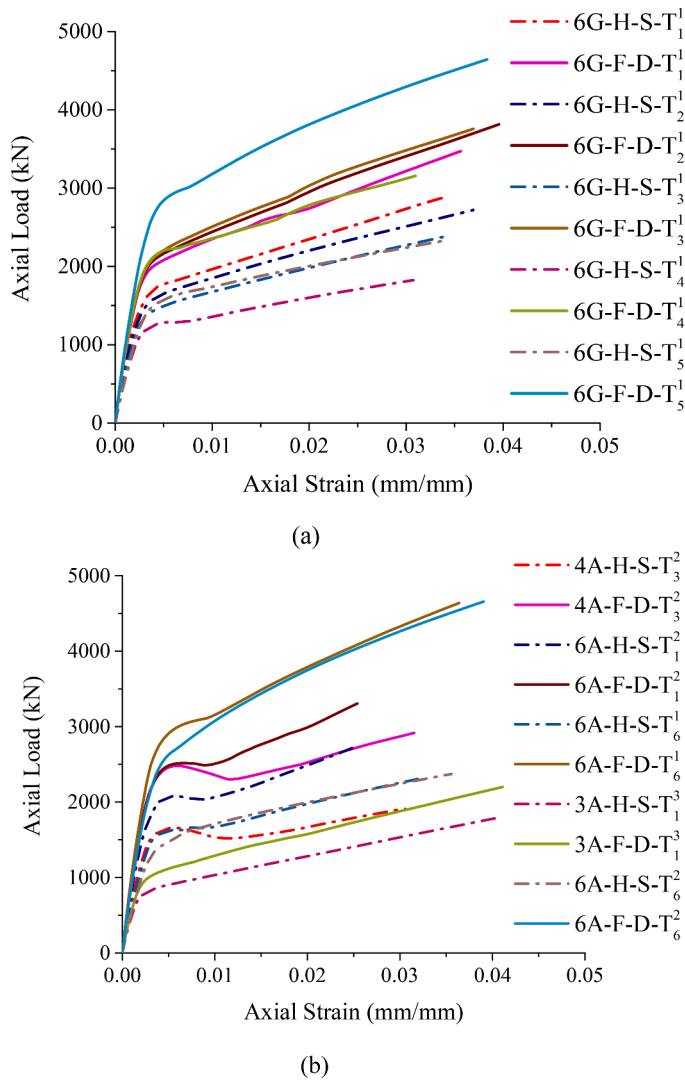


Fig. 12. Effect of double steel tubes on load-strain curve of: (a) GFRP confinement and (b) AFRP confinement.

3.4. Effect of type of FRP

In this section, we delve into the outcomes of comparing the AFRP and GFRP confined columns, focusing on their ultimate load-carrying capacity and ultimate axial strain response.

As presented in Table 12 and Figs. 18 and 19, the type of the FRP material employed for the confinement considerably impacts the behaviour of the columns. The ultimate load-carrying capacity is a fundamental indicator of a column's structural strength, and it is evident that GFRP-confined columns demonstrate higher load-carrying capacities than their AFRP-confined counterparts.

This observed trend aligns with the mechanical properties of GFRP and AFRP highlighted in Table 2, where GFRP exhibited higher peak tensile strength than AFRP. This higher tensile strength allows GFRP to withstand higher loads before failure, translating into higher load-carrying capacities witnessed in the GFRP-confined columns. Transitioning from AFRP to GFRP confinement leads to a substantial increase in the ultimate load-carrying capacity for both the DSHT and DSDFT columns. The DSHT columns displayed an increase ranging from 4.79–8.12 %, while the DSDFT columns provided improvements ranging from 9.32–13.08 % in the load-carrying capacity. Additionally, the GFRP-confined columns indicated approximately 25 % higher ultimate axial strains compared to the AFRP-confined DSHT and DSDFT columns. This aligns with their distinct mechanical behaviours under the applied loads. GFRP exhibited a higher peak axial strain of 3.21 %, showcasing superior elongation capabilities and enhanced ductility compared to AFRP, which demonstrated a peak axial strain of 1.86 %, as can be seen in Table 2. This observation is consistent with findings reported by Albitar et al. [30], for GFRP and AFRP-confined concrete.

4. ML results and discussion

The FEM investigation has yielded valuable insights into the columns' behaviour, encompassing the impact of variables such as the introduction of double steel tubes, type of FRP confinement, concrete strength, confinement layers, and steel tube dimensions. These insights have laid the groundwork for the formulation and training of the ML models. By assimilating the knowledge garnered from the FEM study, the ML models were endowed with the capacity to comprehend and encapsulate the intricate relationships between the input parameters and output predictions. Through a juxtaposition of the ML predictions against the FEM outcomes, a comparative assessment became feasible, facilitating the determination of the ML models' efficacy in

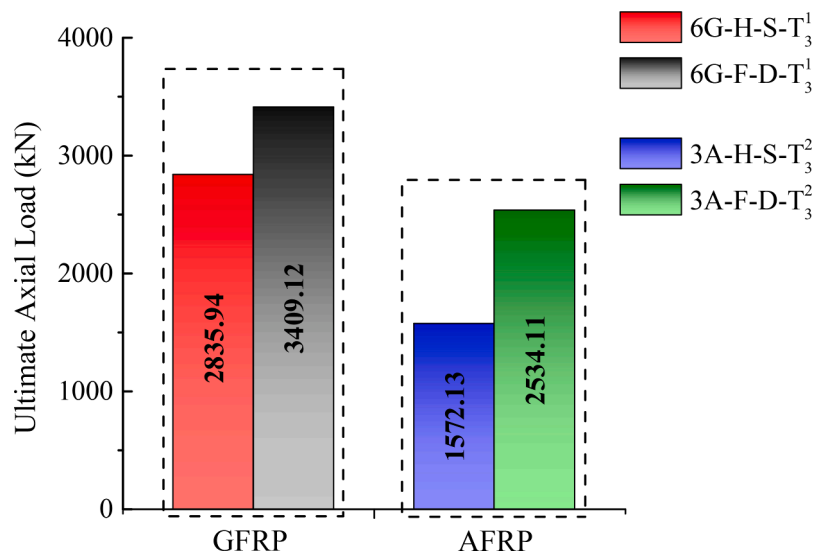


Fig.13. Ultimate axial load of DSHT and DSDFT columns.

Table 10

Comparison of axial load and axial strain for different FRP thicknesses in DSDFT and DSHT columns.

Specimen	Axial load (kN)	Increment (%)	Axial strain (mm/mm)	Increment (%)
4G-F-D-T ₁ ¹	3007.73	15.42	0.0359	-0.83
6G-F-D-T ₁ ¹	3471.55		0.0356	
4G-F-D-T ₂ ¹	3303.90	15.47	0.0404	-1.98
6G-F-D-T ₂ ¹	3815.11		0.0396	
4G-F-D-T ₃ ¹	3290.96	14.18	0.0378	-2.38
6G-F-D-T ₃ ¹	3757.88		0.0369	
4G-F-D-T ₄ ¹	2836.69	11.26	0.0315	-1.58
6G-F-D-T ₄ ¹	3156.37		0.0310	
4G-F-D-T ₅ ¹	4223.11	9.95	0.0392	-2.29
6G-F-D-T ₅ ¹	4643.45		0.0383	
4A-F-D-T ₃ ²	2914.89	13.22	0.0325	-3.07
6A-F-D-T ₃ ²	3300.33		0.0315	
1A-F-D-T ₁ ³	1480.27	48.58	0.0426	-3.52
3A-F-D-T ₁ ³	2199.52		0.0411	
1A-F-D-T ₃ ²	1799.95	40.17	0.0462	-5.41
3A-F-D-T ₃ ²	2523.00		0.0437	
6G-H-S-T ₁ ¹	2903.98	13.31	0.0345	-0.28
8G-H-S-T ₁ ¹	3290.76		0.0344	
6G-H-S-T ₂ ¹	2720.82	13.07	0.0373	-1.07
8G-H-S-T ₂ ¹	3076.69		0.0369	
6G-H-S-T ₃ ¹	2396.09	10.72	0.0345	-3.18
8G-H-S-T ₃ ¹	2653.04		0.0334	
6G-H-S-T ₄ ¹	1824.95	14.31	0.0307	-2.93
8G-H-S-T ₄ ¹	2086.21		0.0298	
6G-H-S-T ₅ ¹	2338.36	12.77	0.0343	-3.20
8G-H-S-T ₅ ¹	2637.01		0.0332	
4A-H-S-T ₃ ²	1907.36	17.56	0.0306	-1.63
6A-H-S-T ₃ ²	2242.33		0.0301	

approximating the load-carrying capacity and ultimate strain of the columns. This holistic evaluation has thereby enabled a comprehensive appraisal of the ML models' performance and their proficiency in replicating the observed behaviour derived from the FEM analysis.

4.1. Prediction results of MARS model

The predictive outcomes of the MARS model are detailed in Table 12. Evidently, the MARS model achieved a R^2 value of 0.918 during the training phase and a R^2 value of 0.900 during the testing phase. This

indicates a comparable performance between the two stages, with an accuracy surpassing 90 %. Further, the precision of error metrics exceeded 94 %, as evident from Table 13, with these values closely aligning with the ideal benchmarks. The regression plot, comparing the actual and predicted values obtained using the MARS model for training and testing, is also presented in Fig. 20, providing a visual insight into the model's performance.

4.2. Prediction results of LS-SVM model

The predictive outcomes of the LS-SVM model are elaborated in Table 14. Evidently, the R^2 value for the LS-SVM model during training is 0.956, while for testing, it stands at 0.904. In comparison to the MARS model, the LS-SVM model displays a higher R^2 value during training. However, during the testing stage, both models indicated equivalent R^2 values, signifying the consistent performance of the MARS model across both phases. In contrast, the LS-SVM model's performance appears to wane during testing. It can be observed from Fig. 21 that the LS-SVM model predicted the values almost similar to the actual values, whereas in the testing stage, significant error in the prediction can be seen.

4.3. Prediction results of LSTM model

The predictive outcomes of the LSTM model are as follows: during training, an exceptional R^2 value of 0.992 was achieved, while during testing, the model maintained an impressive R^2 value of 0.945. These remarkable R^2 values are indicative of the LSTM model's superior predictive capabilities. Complementing this, the error metric value indicated a minimal, nearly zero magnitude, as clearly evident from Table 15. Fig. 22 also establishes that the predicted values are very close to the actual values in the training and testing stages, reaffirming its accuracy and proficiency across both the stages.

4.4. Prediction results of BI-LSTM model

In congruence with the LSTM model, the BI-LSTM model depicts impressive predictive prowess in both the training and testing stages. Notably, the BI-LSTM model illustrates a slightly enhanced predictive performance during the testing phase, surpassing even the commendable results of the LSTM model. This observation underscores the BI-LSTM model's ability to yield more accurate predictions during the testing stage compared to its LSTM counterpart. The results of the prediction are pointed out in Table 16, and the comparison between the actual and predicted values for the BI-LSTM model is shown in Fig. 23.

The predicted values derived from the four distinct models, encompassing both the training and testing phases, are subjected to a comprehensive assessment using Taylor diagrams. These diagrams, serving as statistical evaluation tools, portray standard deviations, correlation coefficients, and RMS differences within a two-dimensional framework. The radial distance from the centre conveys standard deviation, the RMS error corresponds to the deviation between the actual and projected values' units, and the azimuthal angle signifies the correlation coefficient. The proximity to the designated reference point ("Ref") determines the optimal prediction model direction. The Taylor diagrams for both the training and testing stages are demonstrated in Figs. 24 and 25, respectively.

Notably, during the training phase, the LS-SVM, LSTM, and BI-LSTM models highlighted marker positions closer to the "Ref" point, implying their superior performance compared to the MARS model. Similarly, in the testing phase, the MARS and LS-SVM models highlighted positions farther from the reference point compared to the LSTM and BI-LSTM models, confirming the statistical findings.

An additional evaluation metric employed is the accuracy matrix, a novel heat map matrix designed to gauge a model's accuracy across multiple performance metrics [53]. As displayed in Fig. 26, the accuracy

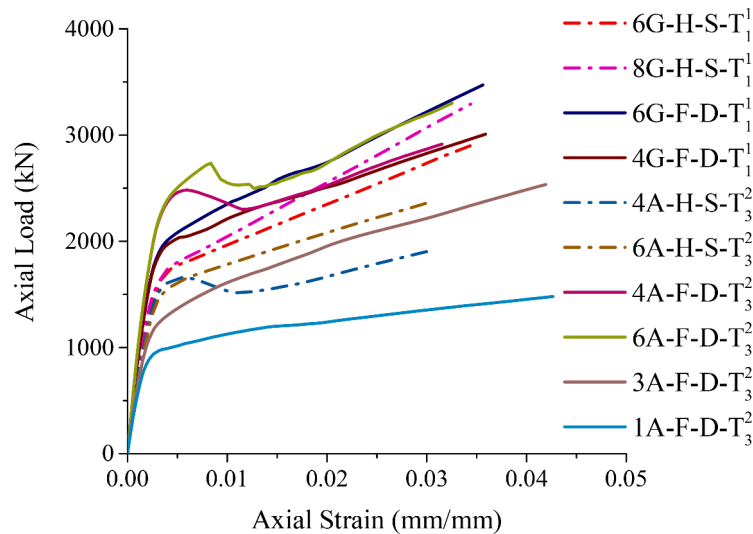


Fig.14. Effect of FRP tube thickness on load-strain curve.

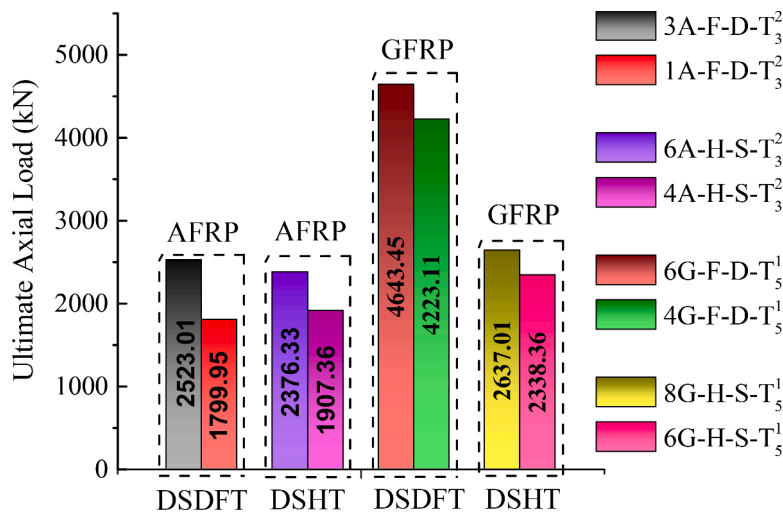


Fig.15. Effect of FRP tube thickness on ultimate axial load of DSHT and DSDFT columns.

Table 11
Comparative analysis of axial load and axial strain with varying steel tube diameters in DSDFT and DSHT columns.

Specimen	Axial load (kN)	Axial strain (mm/mm)	Specimen	Axial load (kN)	Increment (%)	Axial strain (mm/mm)	Increment (%)
6G-H-S-T ₁	2903.98	0.0345	6G-H-S-T ₂	2720.82	-6.31	0.0373	8.11
			6G-H-S-T ₃	2396.09	-17.49	0.0345	0
			6G-H-S-T ₄	1824.95	-37.16	0.0307	-11.01
			6G-H-S-T ₅	2338.36	-19.47	0.0343	-0.01
4G-F-D-T ₁	3007.73	0.0359	4G-F-D-T ₂	3303.90	9.85	0.0404	12.53
			4G-F-D-T ₃	3290.96	9.41	0.0378	5.29
			4G-F-D-T ₄	2836.69	-20.64	0.0315	-12.25
			4G-F-D-T ₅	4223.11	40.41	0.0392	9.19
8G-H-S-T ₁	3290.76	0.0344	8G-H-S-T ₂	3076.69	-6.51	0.0369	7.26
			8G-H-S-T ₃	2653.04	-19.37	0.0334	-2.91
			8G-H-S-T ₄	2086.21	-36.60	0.0298	-13.37
			8G-H-S-T ₅	2637.01	-19.86	0.0332	-3.48

matrix reveals that predictive models (LS-SVM, LSTM, and BI-LSTM) achieve notable accuracy during training. Among these, the MARS model revealed slightly lower accuracy for the performance parameters R^2 and $Adj.R^2$.

In the testing stage, a reduction in the accuracy is evident for the

MARS and LS-SVM models, highlighted by red tones in the accuracy matrix. In contrast, the LSTM and BI-LSTM models sustain their performance during testing, indicated by the yellow tones in the accuracy matrix. Through a comprehensive comparison of the overall performance of the developed models, it can be concluded that, among the

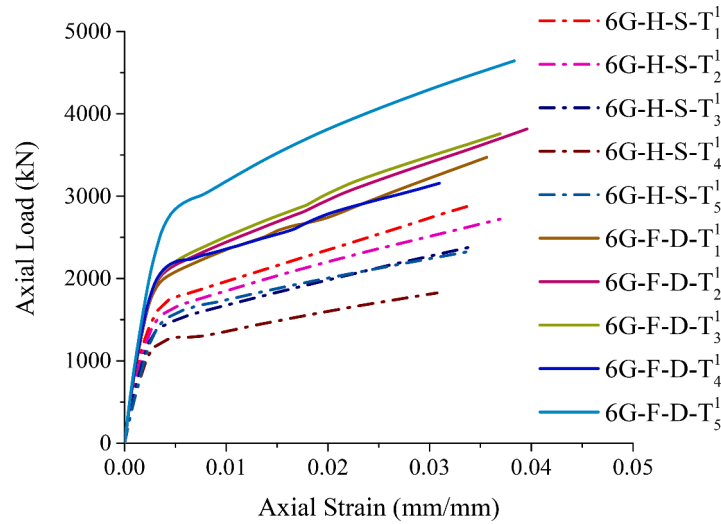


Fig.16. Effect of steel tube diameter on load-strain curve.

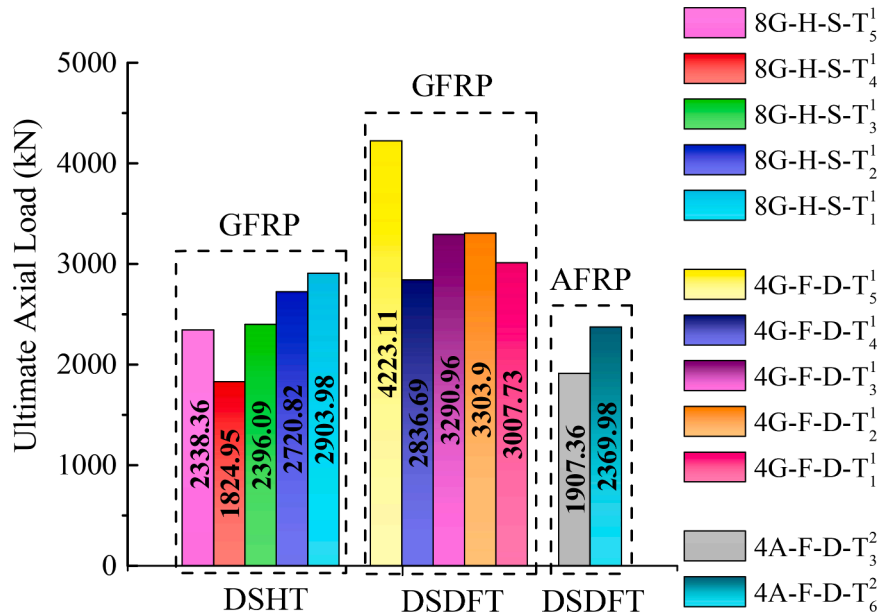


Fig.17. Effect of steel tube diameter on ultimate axial load of DSHT and DSDFT columns.

Table 12

Comparative analysis of axial load and axial strain with different FRP types in DSDFT and DSHT columns.

Specimen	Axial load (kN)	Increment (%)	Axial strain (kN)	Increment (%)
6A-H-S-T ₃ ²	2241.74	4.79	0.0301	29.57
6G-H-S-T ₃ ²	2349.16		0.0390	
6A-H-S-T ₆ ²	2369.98	8.12	0.0356	22.19
6G-H-S-T ₆ ²	2562.43		0.0435	
6A-F-D-T ₃ ²	3300.33	13.08	0.0315	31.74
6G-F-D-T ₃ ²	3732.27		0.0415	
6A-F-D-T ₆ ²	4689.62	9.32	0.0398	23.86
6G-F-D-T ₆ ²	5126.92		0.0493	

four proposed models, the LSTM and BI-LSTM models are well-suited for predicting the results of the considered output. Meanwhile, the MARS and LS-SVM models can satisfactorily predict the output results.

The relationships and interactions between the output and four input variables that were considered in the current study for the ML analysis are explained using the SHapley Additive exPlanations (SHAP) analysis process. Shapley values, which are produced by applying game theory coalitions, are used in the SHAP analysis process to explain the contribution of each feature to each prediction. The SHAP global explanations and mean absolute SHAP values of the BI-LSTM model are depicted in Figs. 27 and 28. It is also evident that increasing Input 1, Input 2, Input 3, and Input 4 will increase the Output, and vice versa, as indicated by the red points (higher values) at the rightmost position in Fig. 27. It can also be seen from Fig. 28 that Input 2 and Input 1 dominate the prediction of output as compared to Input 4 and Input 3. There is a correlation between these observations and the dataset that was used in the research. If there are more data points, then the obtained results will be more accurate.

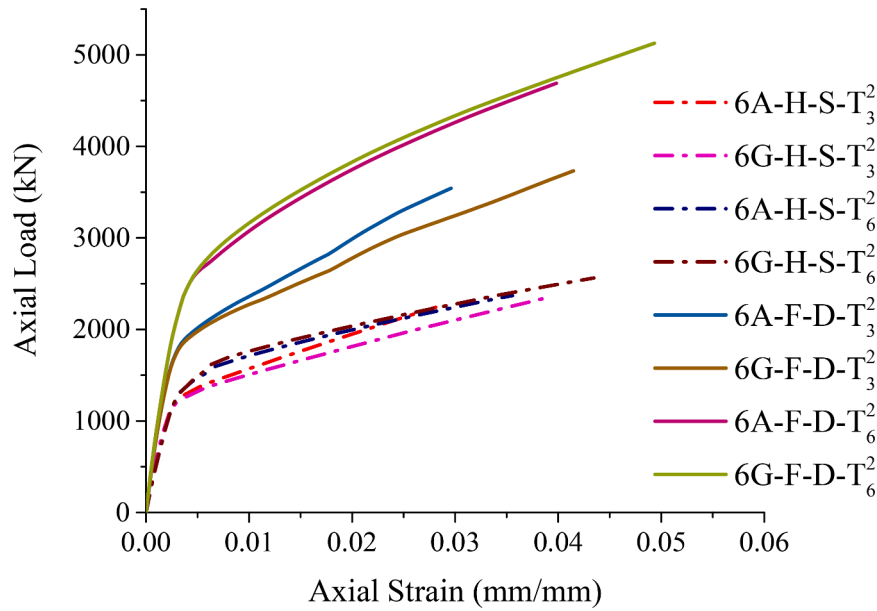


Fig. 18. Effect of FRP type on load-strain curve.

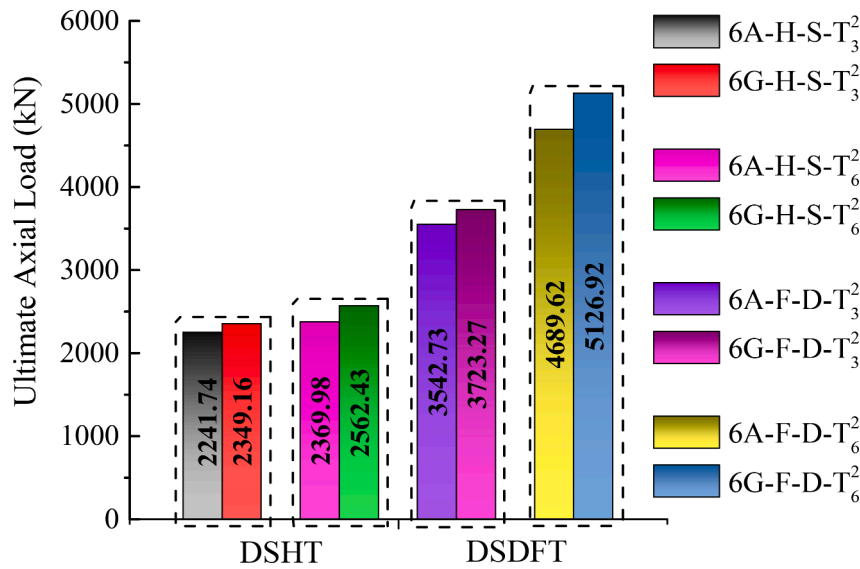


Fig. 19. Effect of FRP type on ultimate axial load of DSHT and DSDFT columns.

Table 13
Prediction performance of MARS.

Index	Metric	Training score	Testing score
1	R^2	0.918	0.900
2	$Adj. R^2$	0.911	0.880
3	RMSE	0.055	0.083
4	MAE	0.046	0.059

5. Conclusions

This study presented a novel configuration of DSDFT columns and investigated the structural behaviour of 48 GFRP and AFRP confined circular DSHT and DSDFT columns using a combination of FEM and ML techniques. The finite element modelling of columns was done using the ABAQUS software. Extensive validation of FEMs against the experimental results of three different research works was conducted ensuring

the accuracy and reliability of the developed models. The study examined the impact of the double steel tube configuration, thickness of FRP, steel tube diameter, and type of FRP on the columns' ultimate axial load-carrying capacity and ultimate axial strain. A dataset of 82 entries forms the basis of the ML models, with the output parameter being the axial load-carrying capacity of the columns. Four different ML algorithms were evaluated for the same. The findings offer valuable insights into the performance of the DSHT and DSDFT columns across various parameters, shedding light on their behaviour. The key findings of the study are:

- Double steel tube configuration: The study highlighted the benefits of employing double steel tubes and concrete infill configuration for enhancing the load-carrying capacity and ductility of the columns. Across different initial steel tube diameters, the DSDFT columns exhibited 19.54 % to 101.21 % increases in the ultimate axial load compared to the DSHT columns. The DSDFTs' additional inner steel tube and concrete infill enhanced load redistribution, confinement effects, and structural integrity. Additionally, the DSDFT columns

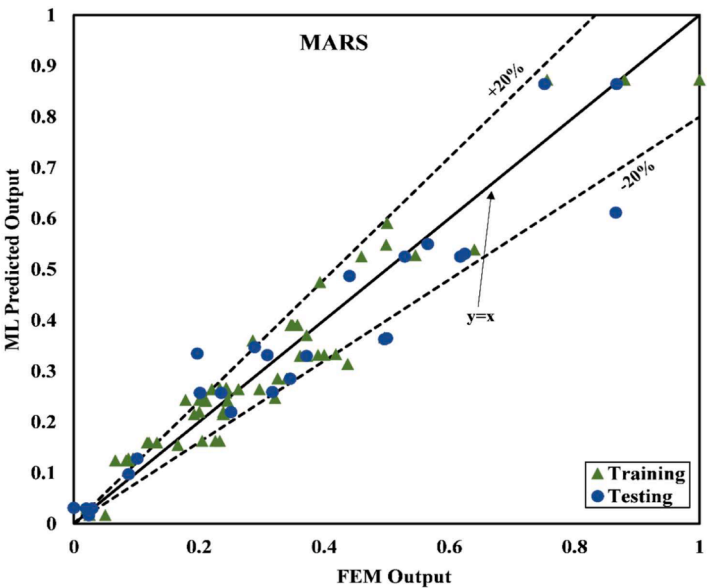


Fig. 20. Regression plot of MARS model for training and testing.

Table 14
Prediction performance of LS-SVM.

Index	Metric	Training score	Testing score
1	R^2	0.956	0.904
2	$Adj.R^2$	0.952	0.885
3	RMSE	0.041	0.086
4	MAE	0.030	0.063

demonstrated higher ductility, as seen at an outer steel tube diameter of 60.3 mm with a 3.18 % increase in the ultimate axial strain compared to the DSHT. The DSFT columns provided substantial enhancements in the load-carrying capacity and ductile behaviour, promising advancements in structural engineering applications. Industries can consider incorporating this configuration in structural

design to maximise the performance of confined columns under the axial compression. This approach could be particularly useful in applications where the load-carrying capacity and deformation behaviour are critical, such as in high-rise buildings or seismic-resistant structures.

Table 15
Prediction performance of LSTM.

Index	Metric	Training score	Testing score
1	R^2	0.992	0.945
2	$Adj.R^2$	0.992	0.934
3	RMSE	0.017	0.065
4	MAE	0.013	0.050

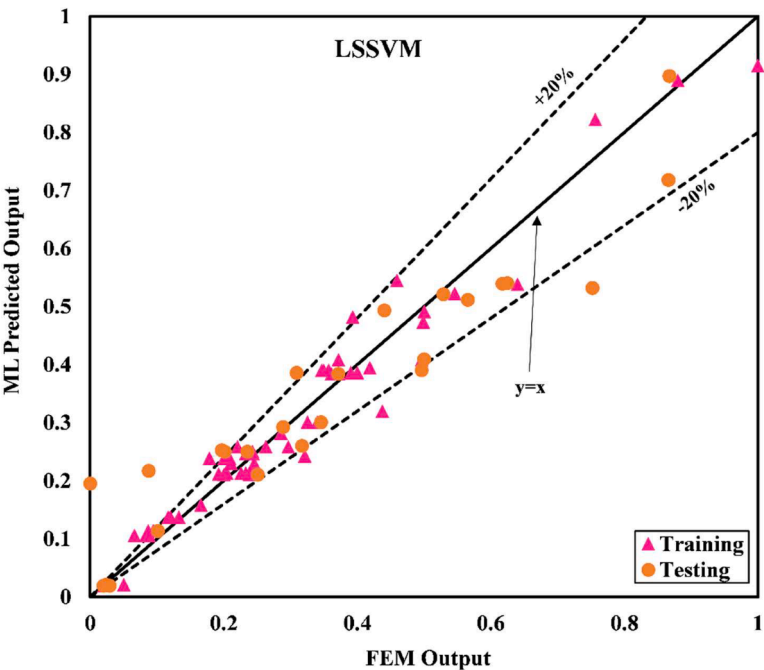


Fig. 21. Regression plot of LS-SVM model for training and testing.

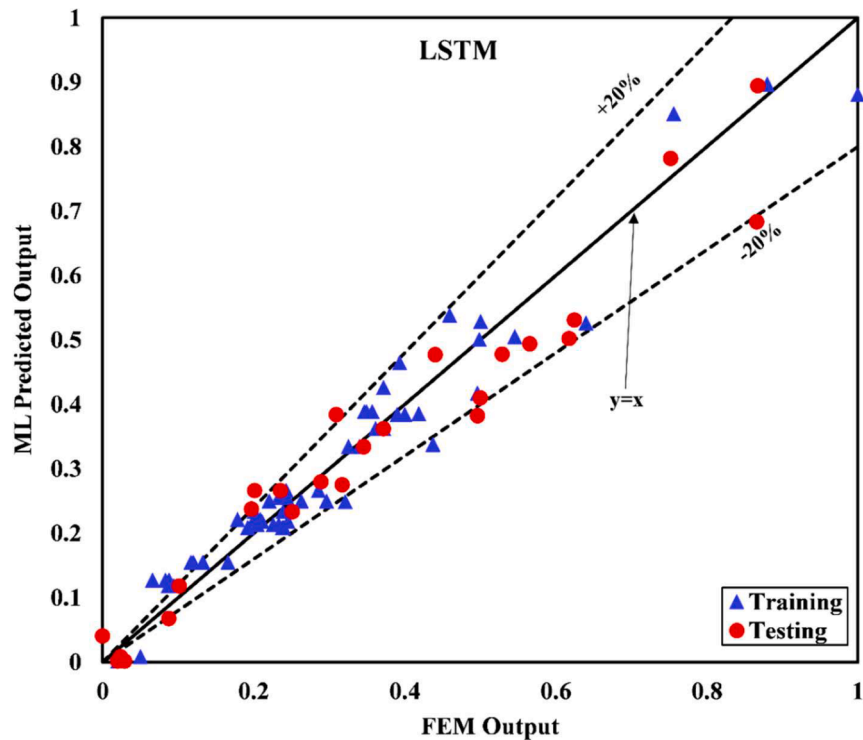


Fig. 22. Regression plot of LSTM model for training and testing.

Table 16
Prediction performance of BI-LSTM.

Index	Metric	Training score	Testing score
1	R^2	0.991	0.955
2	$Adj. R^2$	0.991	0.946
3	RMSE	0.018	0.057
4	MAE	0.013	0.044

b) FRP layer thickness optimisation: The investigation indicated the influence of the GFRP and AFRP layers' thickness on the load-carrying capacity and ultimate axial strain. Increases in the thickness of the GFRP layers notably boosted the ultimate axial load by 10 % to 14 % in the DSHT columns, and 10 % to 15 % in the DSDFT columns. For the AFRP layers, the increase in the ultimate axial load-carrying capacity was up to 18 % for the DSHT columns and up to 40 % for the DSDFT columns. However, the increased thickness brought heightened stiffness, limiting the deformation potential correlating with a reduction in the ultimate axial strain by 4 % to 5 %. Industries

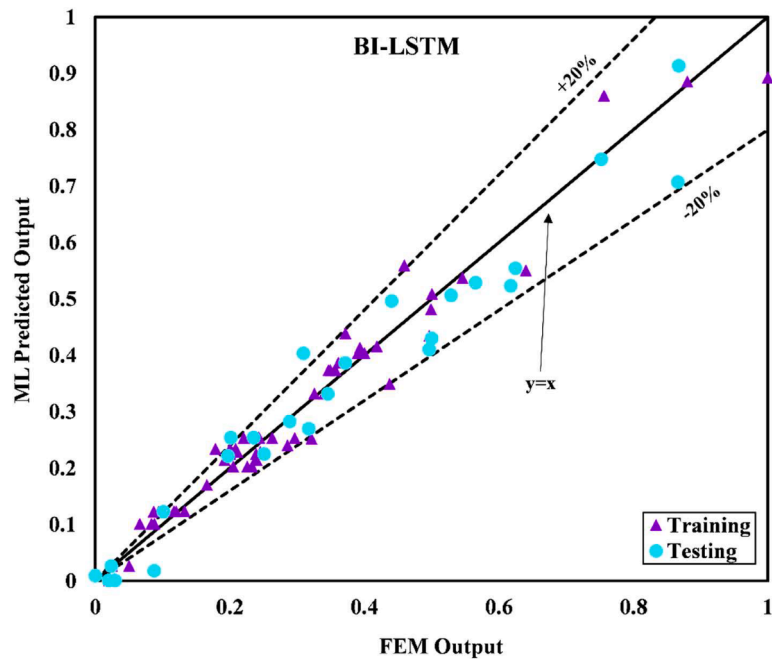


Fig. 23. Regression plot of BI-LSTM model for training and testing.

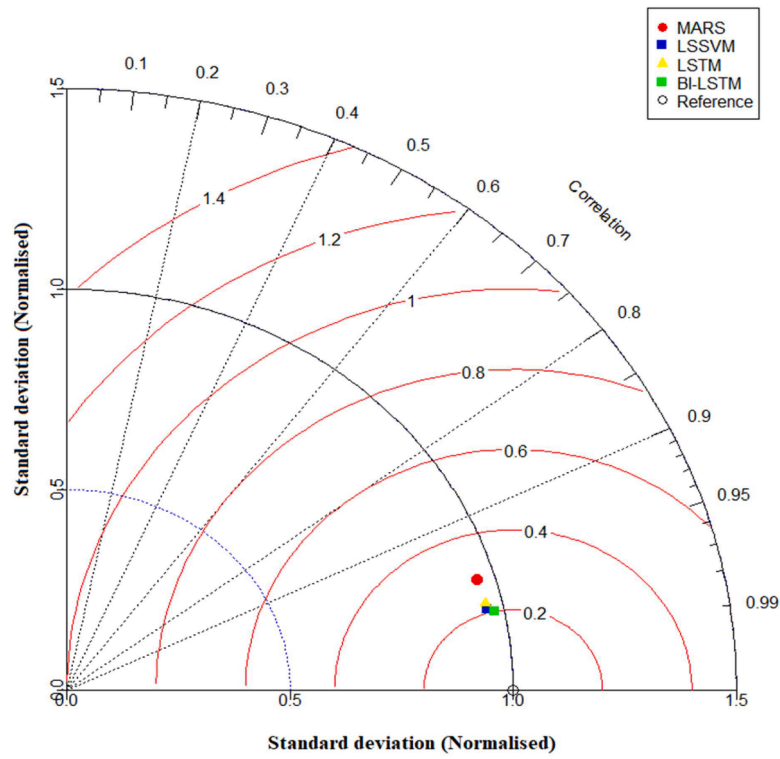


Fig. 24. Taylor diagram for training stage.

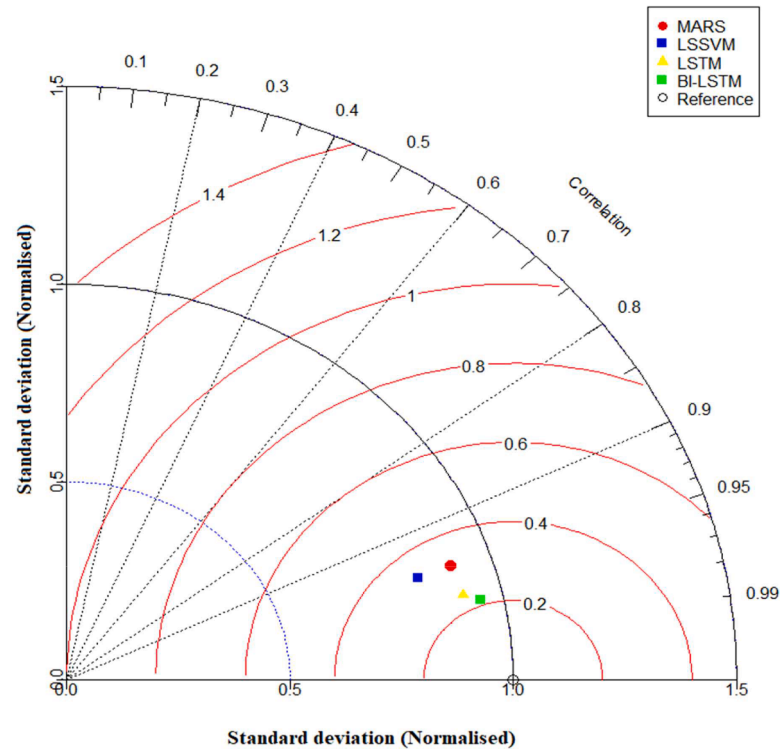


Fig. 25. Taylor diagram for testing stage.

can leverage this insight to fine-tune the number of FRP layers in confined columns based on specific project requirements. Designers can select an appropriate thickness to achieve desired load-carrying capacities while considering the potential trade-offs with the ductility.

c) Selection of FRP material: The comparison between the AFRP and GFRP confined columns highlights pivotal differences in the ultimate load-carrying capacity and axial strain response. The GFRP-confined columns consistently exhibited 5 % to 13 % higher load-carrying capacities and 25 % higher ultimate axial strain than their AFRP

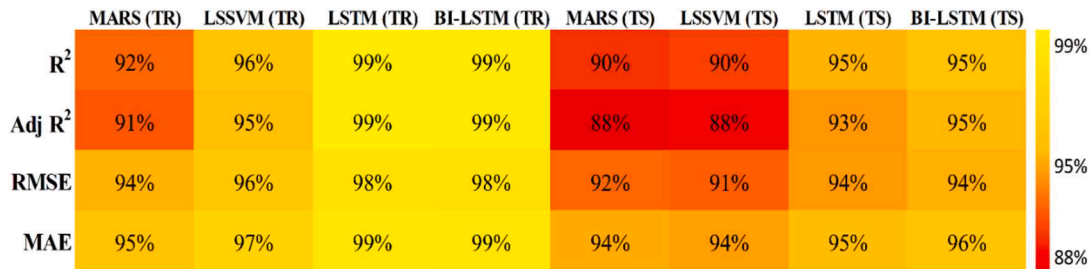


Fig. 26. Accuracy matrix of ML models for output 1 for training and testing stages.

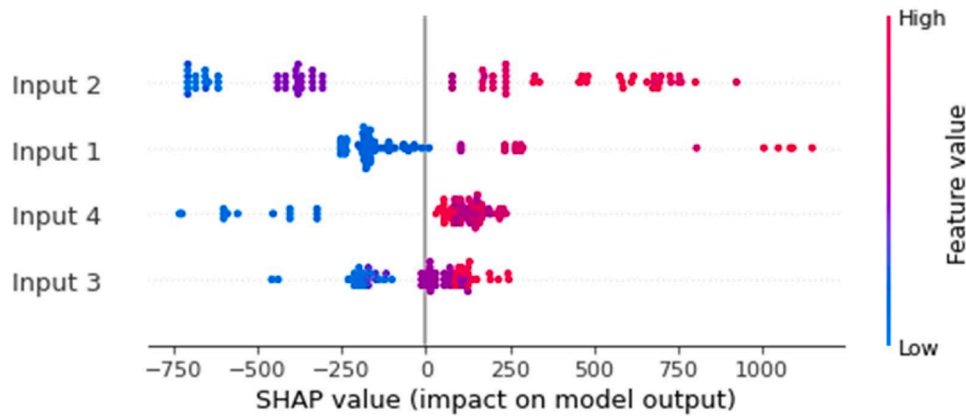


Fig. 27. SHAP global explanation for output from BI-LSTM model.

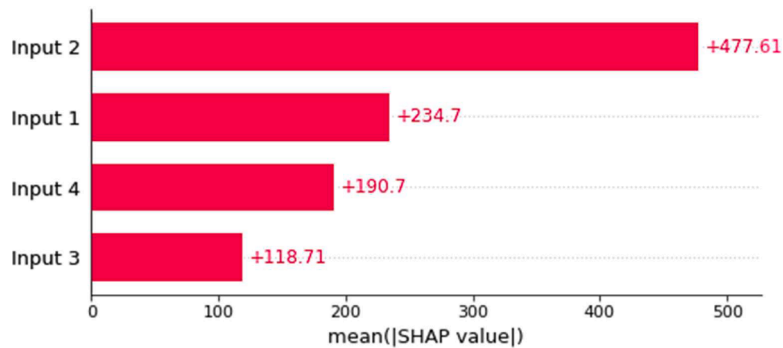


Fig. 28. Mean absolute SHAP values for output from BI-LSTM model.

- counterparts, in line with the GFRP's superior peak tensile strength and peak axial strain. In industrial applications where structural strength and deformation behaviour are paramount, utilising the GFRP confinement can lead to more robust and resilient structures.
- d) Consideration of steel tube diameter: The study revealed the impact of the steel tube diameter on the confined columns' behaviour. For the DSHT columns, a larger outer steel tube diameter led to a decrement in the ultimate axial load-carrying capacity due to reduced concrete presence between FRP and steel tube. Notably, there was an approximate 37.16 % decrease in the load-carrying capacity, as the steel tube diameter increased from 60.3 mm to 101.6 mm. In contrast, the DSDFT columns exhibited a proportional increase in both the load-carrying capacity and strain with larger outer steel tube diameters. The ultimate axial load-carrying capacity notably rose by about 40.41 %, and the ultimate strain increased by 9.19 % going from 60.3 mm to 114.6 mm diameter. By carefully selecting the steel tube diameter, designers can optimise the load-carrying capacity while maintaining acceptable levels of ductility.

- e) Structural Retrofitting: The findings can be applied to retrofitting existing structures to enhance their load-carrying capacity and deformation behaviour. By strategically incorporating the insights from this study, industries can revitalise ageing infrastructure while ensuring compliance with modern structural standards.
- f) ML Models: The analysis assessed four ML models. The MARS model consistently achieved over 90 % accuracy, while the LS-SVM model showed higher training R^2 but decreased in testing. In contrast, the LSTM and BI-LSTM models maintained exceptional accuracy across both phases, with the latter slightly outperforming the former. Evaluation tools confirmed LSTM and BI-LSTM superiority, especially in testing, while the SHAP analysis highlighted Input 1 and Input 2's crucial role in the predictions. Overall, LSTM and BI-LSTM stood out for accurate predictions, while MARS and LS-SVM performed adequately.

Funding

This research received no external funding.

CRediT authorship contribution statement

Liaqat Ali: Data curation, Formal analysis, Investigation, Methodology, Software, Validation, Visualization, Writing – original draft, Writing – review & editing. **Haytham F. Isleem:** Conceptualization, Data curation, Formal analysis, Investigation, Methodology, Project administration, Resources, Software, Supervision, Validation, Visualization, Writing – original draft, Writing – review & editing. **Alireza Bahrami:** Conceptualization, Data curation, Formal analysis, Investigation, Methodology, Project administration, Resources, Software, Supervision, Validation, Visualization, Writing – original draft, Writing – review & editing. **Ishan Jha:** Data curation, Formal analysis, Investigation, Methodology, Software, Validation, Visualization, Writing – original draft, Writing – review & editing. **Guang Zou:** Conceptualization, Data curation, Formal analysis, Investigation, Methodology, Project administration, Resources, Software, Supervision, Validation, Visualization, Writing – original draft, Writing – review & editing. **Rakesh Kumar:** Data curation, Formal analysis, Investigation, Methodology, Software, Validation, Visualization, Writing – original draft, Writing – review & editing. **Abdellatif M. Sadeq:** Data curation, Formal analysis, Investigation, Methodology, Software, Validation, Visualization, Writing – original draft, Writing – review & editing. **Ali Jahami:** Data curation, Formal analysis, Investigation, Methodology, Software, Validation, Visualization, Writing – original draft, Writing – review & editing.

Declaration of competing interest

The authors declare that they have no known competing financial interests or personal relationships that could have appeared to influence the work reported in this article.

Data availability

Data will be made available on request.

References

- [1] S.P. Rashid, A. Bahrami, Structural performance of infilled steel-concrete composite thin-walled columns combined with FRP and CFRP: A comprehensive review, *Materials* 16 (4) (2023) 1564.
- [2] A. Bahrami, S.P. Rashid, A state-of-the-art review on axial compressive behavior of concrete-filled steel tubes incorporating steel fiber and GFRP jacketing, *Buildings* 13 (3) (2023) 729.
- [3] L.C. Hollaway, J.G. Teng, Strengthening and rehabilitation of civil infrastructures using fibre reinforced polymer (FRP) composites, Woodhead Publishing, Cambridge, 2008.
- [4] M. Motavalli, C. Czaderski, FRP composites for retrofitting of existing civil structures in Europe: state-of-the-art review, in: Proceedings, International conference of composites and polycon, American composites manufacturers association, Florida, 2007, pp. 1–10.
- [5] L.C. Bank, Composites for construction: Structural design with FRP Materials, John Wiley & Sons, West Sussex, 2006.
- [6] A. Ahmad, A. Bahrami, O. Alajarmeh, N. Chairman, M. Yaqub, Investigation of circular hollow concrete columns reinforced with GFRP bars and spirals, *Buildings* 13 (4) (2023) 1056.
- [7] T. Ozbakkaloglu, Axial compressive behavior of square and rectangular high-strength concrete-filled FRP tubes, *J. Compos. Constr.* 17 (1) (2013) 151–161.
- [8] T. Ozbakkaloglu, Concrete-filled FRP tubes: Manufacture and testing of new forms designed for improved performance, *J. Compos. Constr.* ASCE 17 (2) (2013) 280–281.
- [9] H.F. Isleem, D.S. Augustino, A.S. Mohammed, A.M. Najemalden, P. Jagadesh, S. Qaidi, M.M.S. Sabri, Finite element, analytical, and artificial neural network (ANN) models for CFRP-confined concrete-filled steel columns with elliptical cross section, *Front. Mater.* 9 (2023) 818.
- [10] H.F. Isleem, F. Peng, B.A. Tayeh, Confinement model for LRS FRP-confined concrete using conventional regression and artificial neural network techniques, *Compos. Struct.* 279 (2022) 114779.
- [11] R. Realforzo, A. Napoli, Results from cyclic tests on high aspect ratio RC columns strengthened with FRP systems, *Constr. Build. Mater.* 37 (2012) 606–620.
- [12] H.F. Isleem, M. Abid, S. Zeb, M. Jize, Analysis of axially loaded columns strengthened with fibre-reinforced polymer, in: Proceedings of the institution of civil engineers-structures and buildings, 2021, pp. 1–23.
- [13] L. Lam, J.G. Teng, Design-oriented stress-strain model for FRP-confined concrete, *Constr. Build. Mater.* 17 (6–7) (2003) 471–489.
- [14] J.G. Teng, T. Jiang, L. Lam, Y.Z. Luo, Refinement of a design-oriented stress-strain model for FRP-confined concrete, *J. Compos. Constr.* 13 (4) (2009) 269–278.
- [15] J.G. Teng, T. Yu, Y.L. Wong, Behaviour of hybrid FRP concrete-steel double-skin tubular columns, in: Proceedings, Second international conference on FRP composites in civil engineering, Adelaide, 2004, pp. 811–818.
- [16] J.G. Teng, T. Yu, Y.L. Wong, S.L. Dong, Hybrid FRP-concrete steel tubular columns: Concept and behavior, *Constr. Build. Mater.* 21 (4) (2007) 846–854.
- [17] T. Yu, Y.L. Wong, J.G. Teng, S.L. Dong, S.S. Lam, Flexural behaviour of hybrid FRP-concrete-steel double skin tubular members, *J. Compos. Constr.* 10 (5) (2006) 443–452. ASCE.
- [18] Y.L. Wong, T. Yu, J.G. Teng, S.L. Dong, Behavior of FRP-confined concrete in annular section columns, *Compos. Part B Eng.* 38 (2008) 451–466.
- [19] G.P. Chen, Y.L. Wang, T. Yu, B.L. Wan, B. Zhang, Q. Liu, Behavior and design-oriented model for elliptical FRP-confined concrete under axial compression, *Eng. Struct.* 249 (2021) 113387.
- [20] A. Bahrami, W.H. Wan Badaruzzaman, S.A. Osman, Structural behaviour of tapered concrete-filled steel composite (TCFSC) columns subjected to eccentric loading, *Comp. Concr.* 9 (6) (2012) 403–426.
- [21] A. Bahrami, W.H. Wan Badaruzzaman, S.A. Osman, Performance of axially loaded tapered concrete-filled steel composite slender columns, *J. Civil Eng. Manage.* 19 (5) (2013) 705–717.
- [22] H.T. Thai, Machine learning for structural engineering: A state-of-the-art review, *Structures* 38 (2022) 448–491.
- [23] I. Jha, K.K. Pathak, Synergetic concrete shape and cable layout optimization of prestressed concrete beams, *Struct. Multidisc. Optim.* 66 (4) (2023) 1–13.
- [24] R.K. Agrahari, I. Jha, K.K. Pathak, Seismic acceleration amplification factor for pin supported moment resisting RC frame structures for Chi-Chi earthquake, *Ind. J. Eng. Mater. Sci.* 29 (2) (2022) 189–200.
- [25] H.F. Isleem, B.A. Tayeh, M. Abid, M. Iqbal, A.M. Mohamed, M.G.E. Sherbiny, Finite element and artificial neural network modeling of FRP-RC columns under axial compression loading, *Front. Mater.* 9 (2022) 288.
- [26] I. Jha, K.K. Pathak, Fuzzy-based integrated zero-order shape optimization of steel-concrete-steel sandwich beams, *Curr. Sci.* 121 (7) (2021) 941–949.
- [27] H.F. Isleem, J.P.J. Ahmad, S. Qaidi, F. Althoei, H.M. Najm, M.M.S. Sabri, Finite element and analytical modelling of PVC-confined concrete columns under axial compression, *Front. Mater.* 9 (2022) 1011675.
- [28] B.A. Louk Fanggi, T. Ozbakkaloglu, Behavior of hollow and concrete-filled FRP-HSC and FRP-HSC-steel composite columns subjected to concentric compression, *Adv. Struct. Eng.* 18 (5) (2015) 715–738.
- [29] B.A. Louk Fanggi, T. Ozbakkaloglu, Compressive behavior of aramid FRP-HSC-steel double-skin tubular columns, *Constr. Build. Mater.* 48 (2013) 554–565.
- [30] M. Albitar, T. Ozbakkaloglu, B.A. Louk Fanggi, Behavior of FRP-HSC-Steel double-skin tubular columns under cyclic axial compression, *J. Compos. Constr.* 19 (2) (2015) 04014041.
- [31] B. Binici, An analytical model for stress-strain behavior of confined concrete, *Eng. Struct.* 27 (7) (2005) 1040–1051.
- [32] S. Prakash, A. Belarbi, Y.M. You, Seismic performance of circular RC columns subjected to axial force, bending, and torsion with low and moderate shear, *Eng. Struct.* 32 (1) (2010) 46–59.
- [33] B. Alfarah, F. López-Almansa, S. Oller, New methodology for calculating damage variables evolution in plastic damage model for RC structures, *Eng. Struct.* 132 (2017) 70–86.
- [34] O. Youssf, M.A. ElGawady, J.E. Mills, X. Ma, Finite element modelling and dilation of FRP-confined concrete columns, *Eng. Struct.* 79 (2014) 70–85.
- [35] ACI 363, State-of-the-art report on high-strength concrete (ACI 363R-92), in: American Concrete Institute Journal Proceedings 81, 1984, pp. 364–411.
- [36] A. Hassan, M. Arif, M. Shariq, Use of geopolymers concrete for a cleaner and sustainable environment—a review of mechanical properties and microstructure, *J. Clean. Prod.* 223 (2019) 704–728.
- [37] Dassault Systemes Simulia Corpia Corp, ABAQUS/Standard User's Manual, Version 6.9, 2020.
- [38] M.Z. Afifi, H.M. Mohamed, B. Benmokrane, Strength and axial behavior of circular concrete columns reinforced with CFRP bars and spirals, *J. Compos. Constr.* 18 (2) (2014) 04013035.
- [39] H.F. Isleem, B.A. Tayeh, W.S. Alaloul, M.A. Musarat, A. Raza, Artificial neural network (ANN) and finite element (FEM) models for GFRP-reinforced concrete columns under axial compression, *Materials* 14 (23) (2021) 7172.
- [40] Z. Tao, Z.B. Wang, Q. Yu, Finite element modelling of concrete-filled steel stub columns under axial compression, *J. Constr. Steel. Res.* 89 (2013) 121–131.
- [41] M. Kumar, B. Biswas, D.R. Kumar, T. Pradeep, P. Samui, Metaheuristic models for the prediction of bearing capacity of pile foundation, *Geomech. Eng.* 31 (2) (2022) 129–147.
- [42] D.R. Kumar, P. Samui, A. Burman, Prediction of probability of liquefaction using soft computing techniques, *J. Instit. Eng. (India): Series A* 103 (4) (2022) 1195–1208.

- [43] J.H. Friedman, Multivariate adaptive regression splines, *Ann. Stat.* 19 (1) (1991) 1–67.
- [44] W. Zhang, C. Wu, Y. Li, L. Wang, P. Samui, Assessment of pile drivability using random forest regression and multivariate adaptive regression splines, in: *Georisk: Assessment and Management of Risk for Engineered Systems and Geohazards*, 15, 2021, pp. 27–40.
- [45] V. Vapnik, *The nature of statistical learning theory*, Springer Science & Business media, 1999.
- [46] K. Greff, R.K. Srivastava, J. Koutník, B.R. Steunebrink, J. Schmidhuber, LSTM: a search space odyssey, *IEEE Trans. Neural Netw. Learn. Syst.* 28 (10) (2016) 2222–2232.
- [47] F. Sherratt, A. Plummer, P. Iravani, Understanding LSTM network behaviour of IMU-based locomotion mode recognition for applications in prostheses and wearables, *Sensors* 21 (4) (2021) 1264.
- [48] M.J. Hamayel, A.Y. Owda, A novel cryptocurrency price prediction model using GRU, LSTM and bi-LSTM Mach. Learn. Algorith. 2 (4) (2021) 477–496. AI.
- [49] M. Schuster, K.K. Paliwal, Bidirectional recurrent neural networks, *IEEE Trans. Signal Process.* 45 (11) (1997) 2673–2681.
- [50] K.A. Althelaya, E.S.M. El-Alfy, S. Mohammed, Evaluation of bidirectional LSTM for short-and long-term stock market prediction, in: *2018 9th international conference on information and communication systems (ICICS)*, 2018, pp. 151–156.
- [51] S.U. Yang, Research on network behavior anomaly analysis based on bidirectional LSTM, in: *2019 IEEE 3rd Information technology, networking, electronic and automation control conference (ITNEC)*, 2019, pp. 798–802.
- [52] T. Ozbakkaloglu, B.A. Louk Fanggi, Axial compressive behavior of FRP–concrete–steel double–skin tubular columns made of normal and high–strength concrete, *J. Compos. Constr.* 18 (1) (2013) 04013027. ASCE.
- [53] R. Kumar, B. Rai, P. Samui, A comparative study of prediction of compressive strength of ultra–high performance concrete using soft computing technique, *Struct. Concr.* 24 (4) (2023) 5538–5555.